RAS Techniques and Instruments

RASTAI **2,** 492–509 (2023) https://doi.org/10.1093/rasti/rzad037
Advance Access publication 2023 August 11

Automatically calculating the apparent depths of pits using the Pit Topography from Shadows (PITS) tool

Daniel Le Corre [1,2★] David Mary,[3] Nigel Mason,[1] Jeronimo Bernard-Salas[2] and Nick Cox[2]

[1]*Centre for Astrophysics and Planetary Science, University of Kent, Giles Lane, Canterbury CT2 7NH, UK*
[2]*Centre d'Etudes et de Recherche de Grasse, ACRI-ST, Av. Nicolas Copernic, F-06130 Grasse, France*
[3]*Lagrange UMR 7293, Université Côte d'Azur, Observatoire de la Côte d'Azur, Bd de l'Observatoire CS 34229, F-06304 Nice, France*

Accepted 2023 July 28. Received 2023 July 12; in original form 2023 January 29

ABSTRACT

Pits, or pit craters, are near-circular depressions found in planetary surfaces, which are generally formed through gravitational collapse. Pits will be primary targets for future space exploration and habitability for their presence on most rocky Solar System surfaces and their potential to be entrances to sub-surface cavities. This is particularly true on Mars, where caves have been simulated to harbour stable reserves of ice water across much of the surface. Caves can also provide natural shelter from the high radiation dosages experienced at the surface. Since pits are rarely found to have corresponding high-resolution elevation data, tools are required for approximating their depths in order to find those which are the ideal candidates for follow-up remote investigation and future exploration. The Pit Topography from Shadows (PITS) tool has been developed to automatically calculate the apparent depth of a pit (h) by measuring the width of its shadow as it appears in satellite imagery. The tool requires just one cropped single- or multiband image of a pit to calculate a profile of h along the length of the shadow, thus allowing for depth calculation where altimetry or stereo image data is not available. We also present a method for correcting shadow width measurements made in non-nadir observations for all possible values of emission and solar/satellite azimuth angles. Shadows are extracted using image segmentation in the form of k-means clustering and silhouette analysis. Across 19 shadow-labelled Mars Reconnaissance Orbiter red-band HiRISE images of atypical pit craters (APCs) from the Mars global cave candidate catalogue (MGC^3), PITS detected 99.6 per cent of all shadow pixels (with 94.8 per cent of all detections being true shadow pixels). Following this testing, PITS has been applied to 123 red-band HiRISE images containing 88 APCs, which revealed an improvement in the variation of the calculated h due to emission angle correction, and also found 10 APCs that could be good candidates for cave entrances on Mars due to their h profiles.

Key words: Machine Learning – Algorithms – Mars – Planetary surfaces – Pits – Cave entrances.

1 INTRODUCTION

Pits are circular-to-elliptical depressions on rocky planetary surfaces which are generally formed by the gravitational collapse of surface material (Ferrill, Hargitai & Kereszturi 2015). Pits can often be misconstrued as impact craters due to their circular morphology and negative elevation relative to the surrounding surface. None the less, pits are most distinguishable from impact craters by the clear lack of a raised rim or any ejecta rays – formed by the impact ejecta settling on the surface. Pits can also range from being bowl-shaped – similar to the interior of impact craters – to being either more regularly conical or cylindrical in shape (Ferrill et al. 2015).

There are several proposed mechanisms for how pits are formed on planetary surfaces. 'Pit crater' is a commonly used term for defining a pit that has been created through volcanic, tectonic, or faulting-related processes (van der Bogert, Ashley & Ferrill 2014). Pits can also be formed due to the loss of subsurface volatiles through chemical dissolution, impact melting, or sublimation (Ferrill et al. 2015). Different formation processes, as well as the gravitational attraction of the host planet/moon, can lead to pits of a range of diameters and volumes, though an extraterrestrial pit exceeding 10 km in diameter will instead be known as a 'caldera' (Mouginis-Mark & Rowland 2001). Many of these mechanisms can also result in several pits occurring in linear or sinuous series, often called 'pit chains' (Hagen 2014). For example, a survey of Martian pit chains with diameters greater than 930 m suggested that dilational normal faulting was likely to be their most prominent formation pathway (Wyrick et al. 2004). This is where normal faults are refracted as they pass through unconsolidated layers, causing dilation under the surface (Ferrill & Morris 2003) through which surface material may drain (see Wyrick et al. 2004, fig. 2). By comparing with known terrestrial examples, Lunar and Martian pit chains that indicate the presence of partially intact lava tubes have also been identified (Sauro et al. 2020). Lava tubes are underground conduits that currently or formerly held flowing or solid lava (Gadányi & van der Bogert 2014), which can form pit chains as their roofs collapse. Collapses along a lava tube are commonly called 'skylights' when they appear to have lateral entrances into the conduit (Gadányi & van der Bogert 2014).

★ E-mail: dl387@kent.ac.uk

Pits are not just present on the Moon (Wagner & Robinson 2014, 2021; Sauro et al. 2020) and Mars (Wyrick et al. 2004; Cushing et al. 2007; Cushing, Okubo & Titus 2015), but have also been observed on other Solar System bodies, including Mercury (Gillis-Davis et al. 2009) and Venus (Davey et al. 2013). However, this work will mostly focus on Martian pits for their prominence in Mars Reconnaissance Orbiter (MRO) High Resolution Imaging Science Experiment (HiRISE) satellite imagery, as well as their role as potential entrances to underground caves. Martian pit craters were first proposed as potential cave entrances due to the thermal properties of their interiors resembling that which would be expected of subsurface material (Cushing et al. 2007). Using Mars Odyssey Thermal Emission Imaging System (THEMIS) infrared imagery, the candidate's interiors were found to emit these wavelengths more strongly than the exposed surrounding surface during the night (see Cushing et al. 2007, fig. 4). Since then, MRO Context Camera (CTX) and HiRISE images have been surveyed to produce a data base of possible cave entrances on Mars called the Mars global cave candidate catalogue (MGC^3; Cushing 2015). This catalogue contains the locations of 1062 candidate cave entrances and subdivides them into a number of categories including atypical pit craters (APCs), lava tube skylights, and non-pit-related species. APCs are good candidates for cave entrances due to their vertical or overhanging walls, rather than being more bowl-shaped – similar to those observed by Wyrick et al. (2004).

Caves have long been a target for human space exploration and scientific investigation (Boston et al. 2004), particularly on Mars. Without sufficient shielding, prospective astronauts on the Martian surface will be limited by how long they can spend there due to exposure to cosmic radiation. Over time, this dosage will lead to an increased chance of cancer development, nervous system deterioration, and acute radiation syndrome (Atri et al. 2022). In spite of this, it will likely not be feasible (in terms of fuel and cost) to transport the amount of shielding necessary for protecting human life over long durations. Therefore, underground caves have been identified as one of the 'best solutions' for a Martian habitat for humans, in terms of eliminating the effect of radiation exposure (Atri et al. 2022). One can imagine that the depth to diameter ratio of a cave entrance is likely to increase the amount of shelter from this risk of radiation that is provided. Numerical simulations have also suggested that caves are able to harbour stable ice deposits (i.e. no net loss of ice after one Martian year) across much of the Martian surface (Williams et al. 2010). Such reserves of water ice would be particularly relevant for longer duration crewed missions to Mars, but also for astrobiological investigations. Within the simulation, a variable that increased the propensity for ice stability in a given cave was its ceiling thickness (see Williams et al. 2010, fig. 2). It can be assumed that a larger ceiling thickness will generally require a deeper or more voluminous cave to be unstable enough to lead to a collapse.

Consequently, knowledge of the depths of planetary pits will be relevant for knowing which features to target for follow-up remote observation with higher resolution sensors, as well as which ones to explore for scientific or habitation purposes. Typically, the relative depths of planetary surface features are found in elevation data produced via radar/laser altimetry or from observing shading changes in stereo image pairs. It is the latter method that generally produces Digital Elevation/Terrain Models (DEMs/DTMs) with the highest spatial resolutions. For example, Mars Global Surveyor (MGS) Mars Orbiter Laser Altimeter (MOLA) DEMs have high surface coverage, but only a best spatial resolution of $\approx$460 m per pixel (Som, Greenberg & Montgomery 2008). Whereas DTMs produced from MRO HiRISE stereo image pairs can have resolutions as low as 1 m per pixel (Kirk et al. 2008). Although, in order to produce this form of elevation data, more than one image is required to have been taken of the same region. This also includes significant computational effort to estimate the elevation. It is also impossible to produce accurate stereo DEMs for areas exhibiting similar shading despite changing viewing angles and solar positions, such as Permanently Shadowed Regions (PSRs). Therefore, data sets of such elevation data typically have low coverage over the entire surface. For example, of the 1062 MGC^3 features, only eight were contained within an MRO HiRISE DTM.

A method for estimating the depths of pits that does not require such elevation data is to observe the size of the pit's shadow as it appears in visual satellite imagery. The principle is that a deeper pit will cast a wider shadow than a shallower one, assuming that the Sun is in the same relative position for both features. Wyrick et al. (2004) propose a method for measuring the width of a pit's shadow (S) as a means of calculating its apparent depth (h) – the relative depth at the edge of the shadow – and estimating their volumes by assuming all pits are conical. According to the MGC^3 documentation, a similar approach, as outlined in Cushing et al. (2015), is also 'generally' used to provide estimates for h for all MGC^3 APCs (Cushing 2015). Both Wyrick et al. (2004) and Cushing et al. (2015) manually measure S using GIS software. Although Wyrick et al. (2004) measures S in MGS Mars Orbiter Camera (MOC) wide-angle images, whereas Cushing et al. (2015) does so in HiRISE imagery. Cushing et al. (2015) apply an additional correction to S for all images with an emission angle (ε) greater than 5° by assuming that MRO and the Sun are pointing either due east or west at all times. An explanation of ε and a description of the method by which Wyrick et al. (2004) and Cushing et al. (2015) derive h from a measurement of S is given in Section 3.2.

With large catalogues of pits, such as MGC^3, it is unlikely that elevation data will be available for all features. In these cases, S must be measured manually for each individual pit, in order to determine their depths using current methods. In addition to this, Machine Learning (ML) and Deep Learning (DL) are being used to automatically detect planetary surface features in remote-sensing imagery (Wang et al. 2017; Tertius Bickel et al. 2020; Lagain et al. 2021; Rajaneesh et al. 2022), including work on detecting Martian pits (Nodjoumi, Pozzobon & Rossi 2021). These techniques will serve to bolster existing catalogues and increase their sizes. Therefore, a method of automatically estimating pit depths from visual satellite imagery will be critical.

In this work, we present a publicly available tool that can automatically calculate apparent depths of Martian and Lunar pits by extracting their shadows and measuring the widths. This application, named Pit Topography from Shadows (PITS), is a Python-based framework that only requires a single cropped remote-sensing image to operate. PITS can also work with single- or multiband imagery. Furthermore, the tool can automatically derive profiles of the apparent depths for entire data sets of pits without the need for any manual calculation or elevation data. The main objectives for developing PITS were to: (i) devise an appropriately simple and robust method for automatically measuring shadow widths; (ii) prove that the tool achieves near-human level accuracy; and (iii) ensure that the entire method is quicker to run than it would take a human to complete.

The remainder of this paper is divided into the following sections. Section 2 is a description and justification of the imagery data set used for development and testing of PITS. Section 3 is an outline of the methodology used to automatically produce apparent depth profiles. Section 4 details the testing performance of PITS' automated shadow extraction, as well as the results of applying the tool to a current catalogue of Martian pits. Section 5 discusses these results and the conclusions are presented in Section 6.

2 DATA SET

The PITS tool has been specifically developed for use on remote-sensing visual imagery, due to its availability at high-resolutions and sufficient coverages, as well as for how shadows appear within them. Shadows are expected to be more distinct in imagery taken in visible wavelengths rather than in the infrared range, since some infrared will still be radiated from the surface underneath the shadow. The amount of infrared radiation observed would also vary depending on a number of factors, such as latitude, time of day/Martian year, and meteorology. The focus has also been on ensuring the tool can be used with geo-referenced remote-sensing data. This is because it is essential to know where the analysed pit is present on the surface, especially for automated cave identification.

During development and testing, PITS has been applied to MRO HiRISE Reduced Data Record Version 1.1 (RDRV11) imagery of Mars (McEwan 2007). This data set was chosen for its very high spatial resolution (0.25–0.5 m per pixel) and the fact that its products are already calibrated and map-projected (McEwen et al. 2007). The products in this data set were also known to contain sufficient MGC^3 features such that a well-sized collection of pit images could be created. MRO HiRISE images are available in single-band images taken in red wavelengths (570–830 nm) and multiband colour images comprised of red, blue-green (< 580 nm), and near-infrared (> 790 nm) filtered passes (McEwen et al. 2007).

We selected 19 red-band images (shown side-by-side in Fig. 1) from the MRO HiRISE RDRV11 data set for determining PITS' accuracy when automatically extracting shadows. These images were acquired by finding the MGC^3 APCs that had corresponding HiRISE imagery and selecting the ones which exhibited good variation in size and morphology. MGC^3 APCs were chosen since it was one of the most abundant classes and appeared the most visually synonymous with the definition of a pit. The corresponding pits were also contained in the colour versions of 12 of these 19 red-band images, allowing for comparison between the different data types.

These testing images were manually labelled using polygons in QGIS (QGIS Development Team 2022) to produce georeferenced ESRI shapefiles for validation. The polygons in these 'validation shapefiles' were assigned an attribute field, called 'class', which described what the particular region of pixels represented. A class of 1 was assigned to the largest continuous shadow in the image, which had clearly been cast by the pit's rim. A class of 2 was given to any bright features, which were wholly contained within the shadow polygon. The reasons for labelling bright features are explained in Section 3.1.4. All remaining regions, which constituted the background, were then assigned a class of 0. These polygons were then rasterized such that each pixel in the input image could be compared to see if a correct shadow detection has been made. Fig. 2 gives an example of this labelling procedure for the testing HiRISE image ESP_052638_2020_RED containing MGC^3 feature APC140.

Since PITS extracts shadows from images cropped to the extents of a pit, a functionality exists to automatically crop larger image products using user-inputted rectangular ESRI shapefile labels. Using these 'location shapefiles', as opposed to simply indexing the pixel coordinates, ensures that the results of PITS can be georeferenced to the pit's position on the surface. The location labels must contain the entire pit, while making sure that no other features exhibiting shadows of comparable sizes (such as impact craters) are included. The location shapefiles should also ideally minimize the proportion of the surrounding surface, but different crop sizes were shown to not significantly affect the resulting shadow detection, as long as the above condition was met.

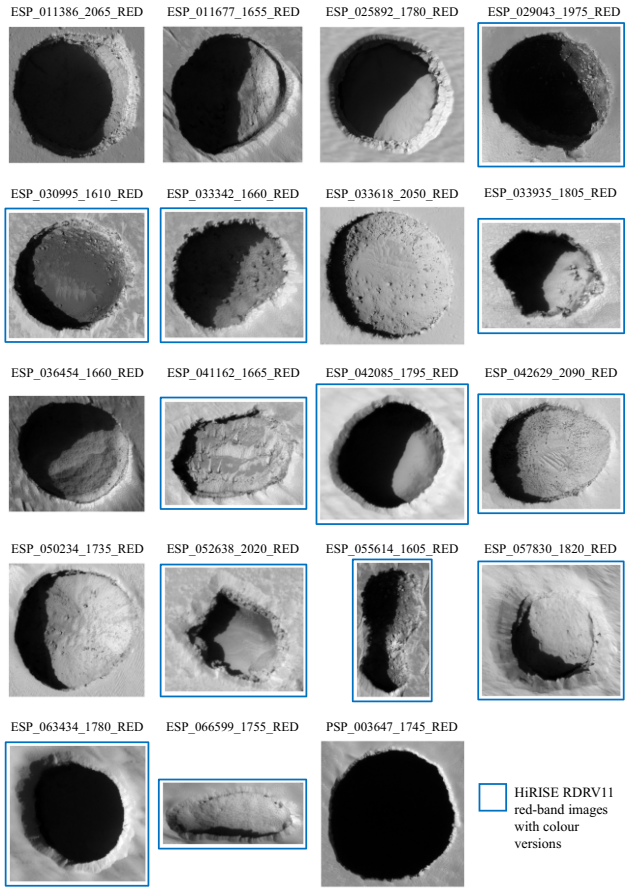

Figure 1. 19 cropped red-band MRO HiRISE Reduced Data Record Version 1.1 (RDRV11) images of MGC^3 APCs. The shadows in these images have been manually labelled in order to assess the performance of the different automated shadow extraction methods detailed in Section 3.1. 12 of these 19 red-band images also have corresponding HiRISE colour versions – denoted by blue outlines. These images are not to scale.

All HiRISE RDRV11 images which contained MGC^3 APCs were acquired in order to compare the depths calculated by PITS with literature estimates. Due to the testing results discussed in Section 4.1, as well as the limited availability of colour versions, only red-band versions were acquired for this depth comparison. From this selection, APCs were removed if they did not exhibit a shadow or if they partially fell outside the images' extents. This resulted in 123 HiRISE observations of 88 MGC^3 APCs, from which PITS extracted the shadows using k-means clustering when maximizing $\bar{s_0}$ (for reasons explained in Sections 4 and 5). A map of the Martian surface overlaid with the locations of the MGC^3 APC features used for both shadow extraction testing and depth comparison can be found in Fig. 3. As well as this depth comparison, a survey was conducted upon these 88 APCs to determine which, if any, were possible cave entrances given the shapes of the h profiles produced by PITS.

3 METHODOLOGY

The following section will detail the various elements of the PITS algorithm that when combined can derive a profile of h along the length of a pit's shadow from a single cropped satellite image. Fig. 4 shows a flow-chart of the whole algorithm that is applied to each input image given to the tool, along with section references for where each step is explained in this work.

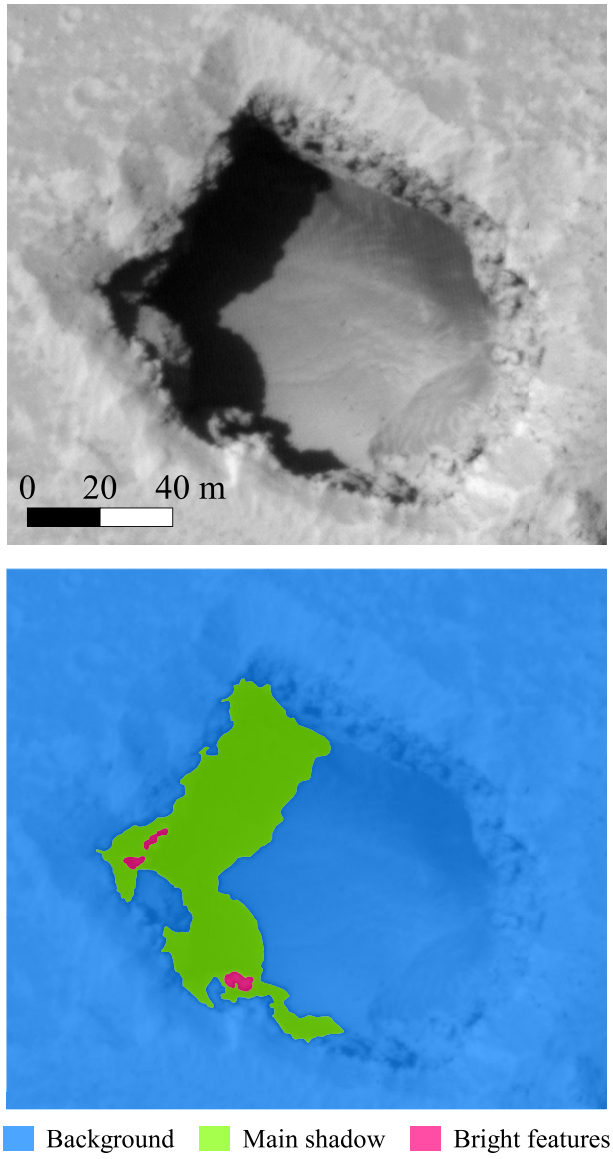

Figure 2. Example of the polygons produced when labelling the testing HiRISE image ESP_052638_2020_RED for the main shadow and any bright regions contained within it, which are likely to be features protruding above the shadow. These polygons were produced in QGIS version 3.4.15 using the 'Advanced Digitizing Toolbar' (QGIS Development Team 2022).

3.1 Automated shadow extraction

As discussed in Section 1, Wyrick et al. (2004) provide a method for estimating the depth of a pit by manually measuring the width of the shadow along the Sun's line of sight in GIS software. In this work, we choose to employ image segmentation to automate this process, whereby a cropped satellite image of a pit would be separated into pixels that contain shadow, and those that are non-shadow background. This would result in a binary shadow mask consisting of detected shadow and background pixels (assigned a 1 and 0, respectively).

Image segmentation methods can range in complexity, from simple thresholding, all the way up to trained semantic/instance segmentation ML or DL models. As mentioned previously, the aim when developing PITS was to devise a method that reflected the simplicity for a human to delineate a shadow. This section details the approaches to image segmentation that were considered for automated shadow extraction: Otsu's method and *k*-means clustering with two different types of silhouette analysis. It also details the necessary post-processing steps, as well as how these methods can be compared to each other on the shadow-labelled images described in Section 2.

3.1.1 Thresholding with Otsu's method

Otsu's method is a non-parametric, unsupervised method of image segmentation which determines a threshold for separating a grey-scale image into foreground and background pixels (Otsu 1979). It does this by finding the threshold which maximizes the interclass variance in intensity between the foreground and background pixels. As shadows should be visibly distinct from the surrounding surface, Otsu's method was considered for use in extracting them.

The full mathematical procedure is as follows: calculate a histogram of the pixel values with L bins, where L is the number of grey levels. The number of pixels in the bin i is given by n_i whilst the total number of pixels is $N = n_1 + n_2 + ... + n_L$. Following Otsu's method, a probability can be assigned to each bin i as $p_i = n_i/N$, where $p_i \geq 0$ and $\sum_{i=1}^{L} p_i = 1$. A given threshold value (t) will separate the pixels into two classes (C_0 and C_1), whose probability distributions are given by equations (1) and (2), respectively.

$$w_1 = \sum_{i=1}^{t} p_i = 1 - w_2, \tag{1}$$

$$w_2 = \sum_{i=t+1}^{L} p_i = 1 - w_1. \tag{2}$$

The mean of classes C_0 and C_1 (μ_1 and μ_2, respectively) are given by equations (3) and (4), where the total mean of all pixels is $\mu_T = w_1\mu_1 + w_2\mu_2$.

$$\mu_1 = \sum_{i=1}^{t} i p_i / w_1, \tag{3}$$

$$\mu_2 = \sum_{i=t+1}^{L} i p_i / w_2. \tag{4}$$

The threshold selected by Otsu's method is the one that maximizes the interclass variance (σ_B^2) of pixels between the two classes, which is given by equation (5).

$$\sigma_B^2 = w_1(\mu_1 - \mu_T)^2 + w_2(\mu_2 - \mu_T)^2. \tag{5}$$

Therefore, any pixels which have an intensity below this threshold are classified as a shadow pixel. It should also be noted that Otsu's method requires a grey-scale image to operate. Therefore, colour images have been averaged across all bands and the averages rounded to produce a single grey-scale image of integer pixel values.

3.1.2 k-means clustering

k-means is an unsupervised clustering algorithm whose objective it is to separate N number of data points into the k number of clusters (defined as $\mathbf{C} = \{C_0, C_1, ..., C_{k-1}\}$) which locally minimize the intracluster sum of squared Euclidean distances. Therefore, *k*-means clustering finds a local minimum of the objective function $J(k)$, given in equation (6), where $\boldsymbol{\mu}_i$ is the mean (also called the 'centroids') of the data points $\mathbf{x}$ in cluster C_i.

$$J(k) = \sum_{i=0}^{k-1} \sum_{\mathbf{x} \in C_i} \|\mathbf{x} - \boldsymbol{\mu}_i\|^2. \tag{6}$$

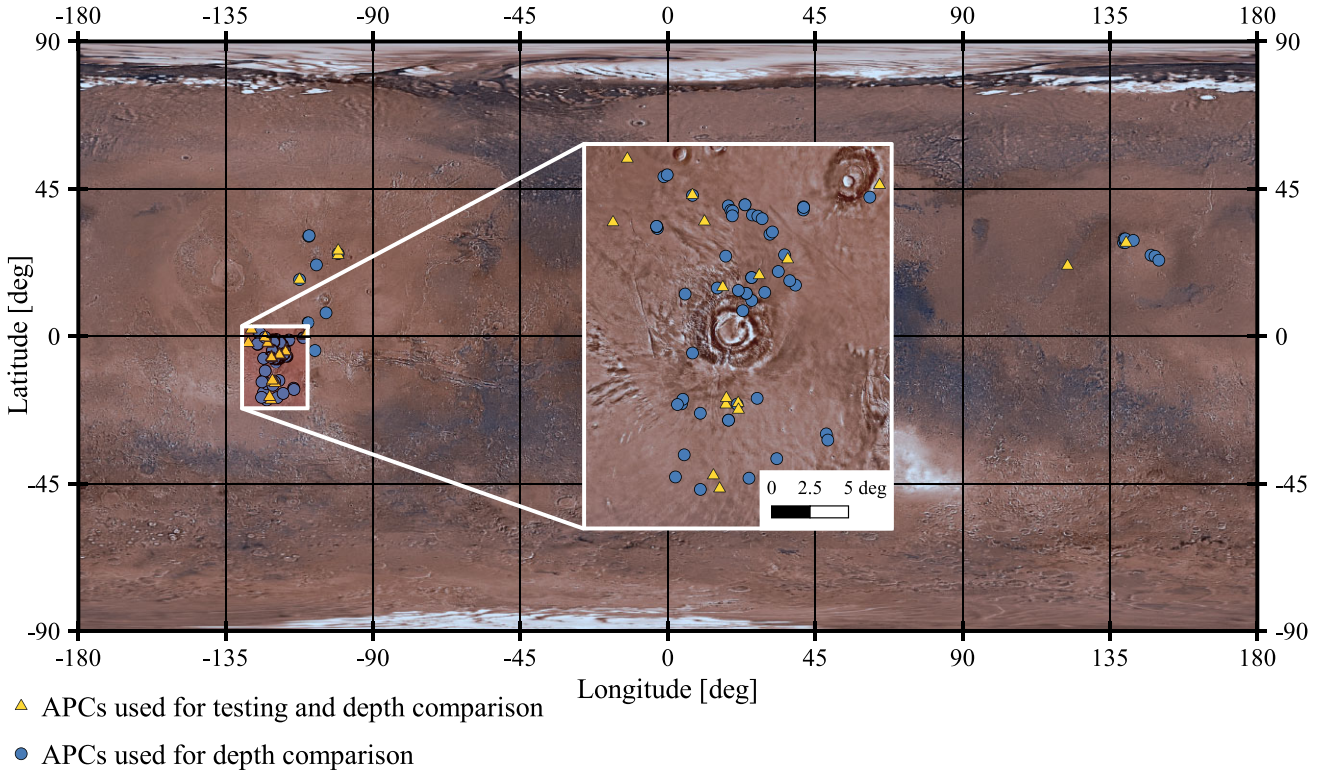

Figure 3. Global map of Mars (in a −180° to 180° longitude domain) showing the 88 MGC[3] APC features that were used in the development of the PITS tool. The 69 APCs which were only used for comparison with the depths provided by MGC[3] are given as blue circles. The 19 APCs which were used both for depth comparison and for testing are given as yellow triangles. The inset axis focuses in on Arsia Mons, since the majority of the APCs used in this work are located there. This map was produced in QGIS by using the USGS Mars Viking Colourised Global Mosaic* as the base map and converting the MGC[3] data base (Cushing 2015) from CSV to ESRI shapefile format with the JMARS GIS software package (Christensen et al. 2009).
* https://astrogeology.usgs.gov/search/map/Mars/Viking/MDIM21/Mars_Viking_MDIM21_ClrMosaic_global_232m.

k-means finds only the local minimum of $J(k)$ since the centroids needs to be initialized – often randomly. Once the centroids have been defined for the first time, the N data points are then each assigned to the cluster to whose centroid it is the closest. These centroids are then iteratively updated by calculating the new mean of the data points $\mathbf{x}$ for each cluster and then repeating this assignment step. This is repeated until the improvement in $J(k)$ no longer meets a given tolerance, or the chosen number of iterations is exhausted. k must also be known a-priori for *k*-means clustering to operate.

k-means clustering was chosen above other clustering methods for its simple-to-interpret procedure and since this algorithm was found to have a suitable run-time when dealing with the high numbers (as well as dimensionality) of data points found in high-resolution remote-sensing imagery. In the case of PITS, the data points that *k*-means must segment are pixel intensities, meaning that the algorithm is tasked with clustering in three dimensions: the longitude, latitude, and pixel intensity axes.

With the implementation of the *k*-means algorithm into PITS, the result is an array of the same size as the input image with each pixel being assigned an integer value according to which cluster it belongs to (0,..., $k-1$). Although, due to how the cluster centroids have to be randomly initialized, these integer values are not assigned consistently across multiple runs even with identical parameters. In order for the tool to extract specific clusters, clusters are reassigned integer values according to their average brightness in the input image (from 0 being the darkest, to $k-1$ the brightest). Only the darkest cluster is then selected, and all constituent pixels are classified as shadow pixels.

In the case of colour images, a single shadow mask had to be derived from the resulting clusters from applying *k*-means to each of the bands. This was performed by clustering each band individually and then taking the modal cluster label for each pixel across the three bands. For example, if a pixel was assigned to clusters C_0, C_1 and C_1 across three bands, then this pixel would be reassigned to the modal cluster of C_1. Where the modal count across all bands for a cluster assigned to a given pixel is 1 or equal to that of another cluster, pixels are preferentially assigned to darker clusters.

3.1.3 *k-means clustering with silhouette analysis*

As was discovered in preliminary testing, using a constant value of k upon all images was resulting in highly variable results. Therefore, a method was necessary for automatically deciding which value of k to use for a given image. This would allow PITS to adapt the *k*-means clustering algorithm to images which may be best described by more or fewer clusters than others.

Silhouette analysis is an approach for automatically suggesting a k value whereby it finds the value of k which returns the clusters whose data points are most consistent and distinct from those in other clusters (Rousseeuw 1987). For simplicity, this can be said to be the k that yields the most appropriate clusters. The degree to which a given data point in cluster C_i is appropriate is defined by the silhouette coefficient (s_i) and is given by equation (7).

$$s_i = \frac{b_i - a_i}{\max\{a_i, b_i\}}, \tag{7}$$

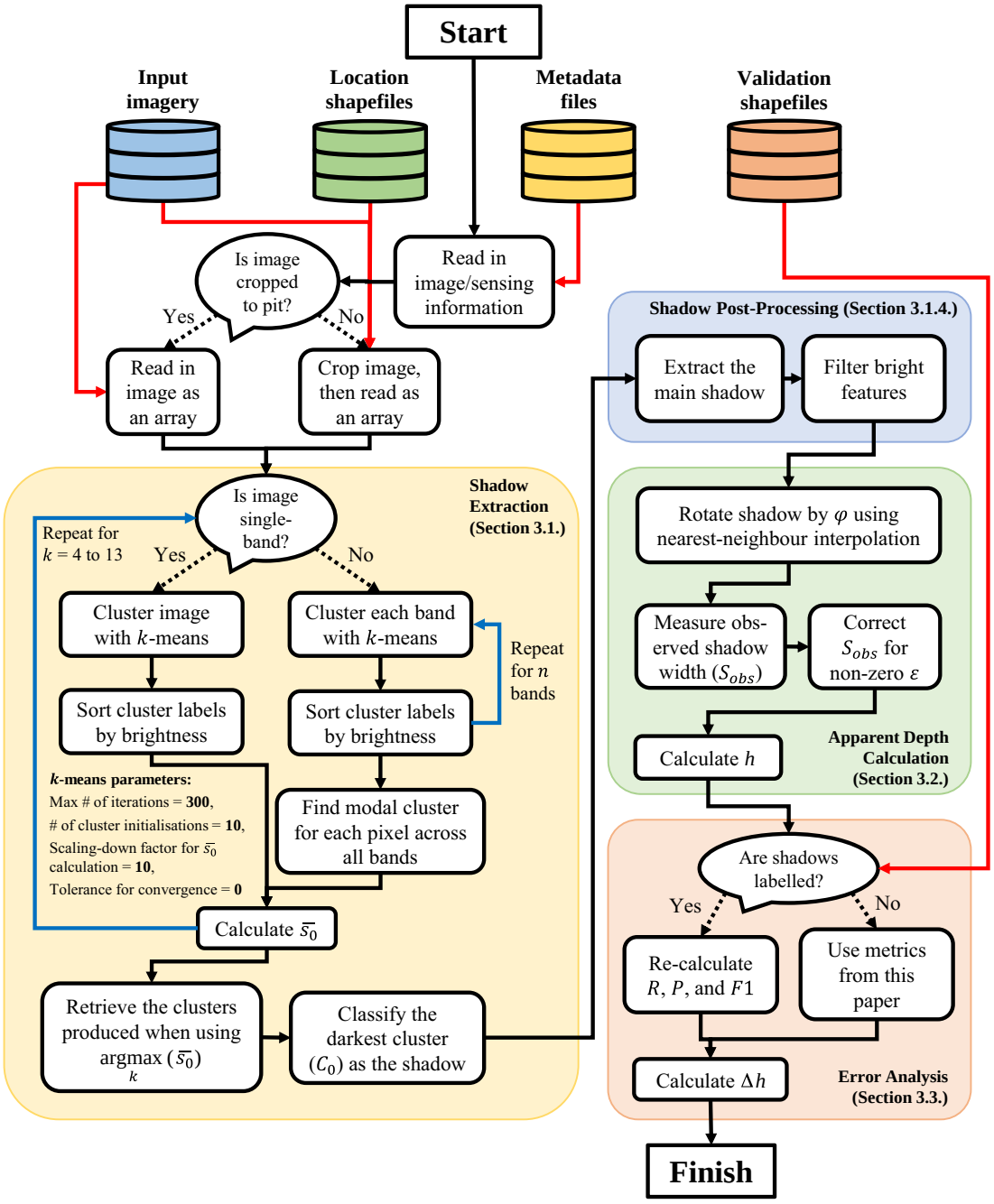

Figure 4. A flow-chart of the entire PITS algorithm. This procedure is applied to each input image given to the tool. Arrows are colour-coded according to the direction of flow through the algorithm (black), when data are retrieved (red), and where there are any iterative processes (blue). Each individual step of the algorithm is stated as a rounded rectangle. Queries which depend upon the type of input data (e.g. whether images are single- or multiband) are given as speech bubbles. All parameters of the PITS algorithm are stated, including the range of k values used for silhouette analysis, the maximum number of iterations of the k-means algorithm, the number of random initializations of cluster centroids, the factor used to scale down images and cluster labels when calculating $\bar{s_0}$, and the tolerance (in squared Euclidean distances) for declaring convergence of the k-means algorithm.

where a_i is the mean distance of a point in cluster C_i to all other points in C_i. Whereas b_i is the shortest mean distance of a point in C_i to all of the points in another cluster which it does not belong to.

s_i can range between -1 and 1, with the goal being to maximize s_i since a larger value corresponds to a more consistent and distinct cluster. This means that instead of applying one value of k, PITS iterates its k-means clustering over a range of k values ($k = 4$ to 13 in integer intervals). This range was selected as testing found that using a smaller or larger k never produced the most accurate results. The tool then calculates s_i for each pixel upon downscaled (by a factor of 10) versions of the input image and the array of assigned cluster values. This factor was chosen since it significantly improves the run-time during this silhouette analysis, while not changing the suggested k values for each image during testing.

s_i is then averaged over all the data points within the same clusters to produce k average silhouette coefficients ($\bar{s_i}$). $\bar{s_i}$ describes, on

average, how consistent all pixels in cluster C_i are with each other and how distinct they are from those in other clusters. The mean of $\bar{s_i}$ can then be taken again, this time to produce an overall silhouette score, which describes how appropriate all clusters are for this value of k. This silhouette analysis has been tested with selecting the value of k that maximized the overall silhouette score and also that which maximized the average silhouette coefficient for the pixels in the darkest cluster ($\bar{s_0}$).

3.1.4 Post-processing of shadow masks

In order to ensure correct shadow width measurement, the extracted shadow masks (produced by Otsu's method and k-means clustering with silhouette analysis) undergo post-processing. Once the binary shadow masks are produced, the largest continuous feature is chosen, while all other smaller shadow detections are removed. The reason for this is to remove any shadows from other objects in the image, such as boulders, which could interfere with the shadow width measurement. The 'main' shadow, upon which the width will be measured, will be the largest shadow, provided the feature is not highly irregular or degraded such that multiple similarly sized shadows are present. This condition is manually verified before using PITS to extract the main shadow in a given image.

Once the main shadow has been found, the next step is to identify any bright features that are wholly contained within it. These are likely to be either noisy pixels, or detritus protruding above the shadow. Whilst any holes in the shadow mask due to the former should be filled, filling in the latter would lead to overestimation in the shadow width since they will be casting their own shadows. As a result, PITS performs morphological closing on all holes with an area less than 10 pixels, such that any remaining larger holes are likely to be protruding bright features.

3.1.5 Comparing automated shadow extraction methods

In order to determine which of the above approaches to automated shadow extraction are most appropriate, a consistent way of comparing them is necessary. All three of (i) Otsu's method, (ii) k-means clustering when maximizing the overall silhouette score, and (iii) k-means clustering when maximizing $\bar{s_0}$ have been applied to the 19 shadow-labelled HiRISE RDRV11 images described in Section 2. Their results have been compared to the rasterized validation shapefiles, whereby a confusion matrix could then be calculated for each image. It should be noted that the results are compared after the shadow has undergone the post-processing described in Section 3.1.4. This matrix consists of the number of true positive (TP), false positive (FP), true negative (TN), and false negative (FN) shadow pixel classifications.

From this matrix, the precision (P), which is the ratio of correctly detected shadow pixels to all detected shadow pixels, is calculated using equation (8).

$$\mathrm{P} = \frac{\mathrm{TP}}{\mathrm{TP} + \mathrm{FP}}. \tag{8}$$

The recall (R), which is defined as the ratio of correctly detected shadow pixels to all true shadow pixels, can also be found using equation (9).

$$\mathrm{R} = \frac{\mathrm{TP}}{\mathrm{TP} + \mathrm{FN}}. \tag{9}$$

A popular metric used for describing the overall performance of classification algorithms is F1 score. As such, F1 score has been selected as the metric for assessing the performance of the various shadow extraction methods. The method that achieves the highest F1 score in detecting shadow pixels is the one chosen for inclusion in the PITS algorithm. F1 score, or just F1, is the harmonic mean of P and R, and is given by equation (10).

$$\mathrm{F1} = 2\left(\frac{\mathrm{P}\cdot\mathrm{R}}{\mathrm{P}+\mathrm{R}}\right). \tag{10}$$

As explained in Section 3.1.3, k-means clustering is performed for a range of k values in order for silhouette analysis to be possible. Therefore, when testing k-means clustering with silhouette analysis, the k values which produced the maximum F1 score in each testing image (not necessarily the one suggested via silhouette analysis) could also be recorded. The F1 scores generated when using these 'target' k values represent the highest achievable performance when using k-means clustering for shadow extraction. This helps assess if silhouette analysis is an appropriate method of automatically suggesting k values. However, they will of course not be known in future instances where the shadows have not been manually labelled.

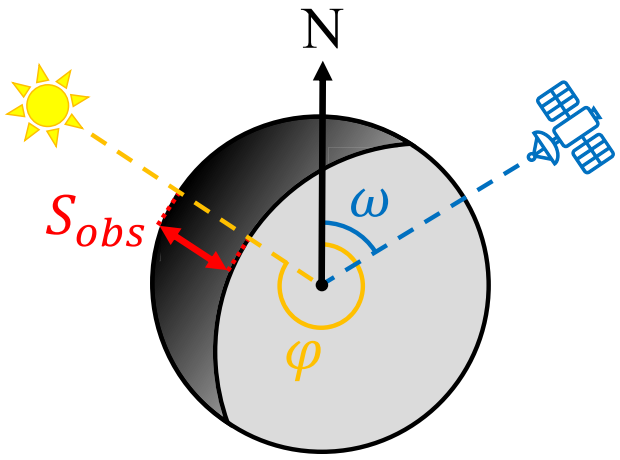

Figure 5. Top-down schematic of an idealized, circular pit, displaying where the observed shadow width (S_{obs}) of a pit along the Sun's line of sight corresponds to when being measured by the PITS tool. The solar azimuth angle (φ) is the clockwise angle between due north (in the case of PITS) and the subsolar point. Similarly, the satellite azimuth angle (ω) is the clockwise angle between the same reference point and the subsatellite point.

3.2 Apparent depth calculation

3.2.1 Automatically measuring shadow widths

The task of manually measuring a shadow's width along the Sun's line of sight is relatively straightforward thanks to map-projected satellite data and GIS software tools. On the other hand, making the same measurement automatically upon the binary shadow masks (extracted via the methodologies in Section 3) is not as simple. This is due to the fact that the Sun's line of sight can come from a range of angles.

In order to account for this, PITS utilizes the solar azimuth angle (φ), which is regularly given in the metadata for planetary remote-sensing imagery. φ is the clockwise angle between some reference point (due north in PITS' case) and the subsolar point – the location directly below the Sun on the surface. Fig. 5 shows how the observed shadow width (S_{obs}), as seen by the HiRISE camera, can be measured by knowing φ.

PITS is able to retrieve φ for each image from the PDS3 index files. These files provide the necessary sensing information for all data products for a particular mission or instrument. Therefore, PITS can rotate the binary shadow masks anticlockwise about their centre by φ to horizontally align the shadow such that the Sun's line of sight now passes directly through the mask from bottom to top. Nearest neighbour interpolation is used when aligning the shadow masks as to return the pixels to a gridded array while retaining their binary values, which would not be the case if a higher order of interpolation was used.

Aligning shadows in this manner means that PITS can now measure the distance between the first and last shadow pixels along the Sun's line of sight (i.e. the shadow pixels adjacent to the pit's rim and shadow's edge, respectively). This shadow width (in pixels) is then multiplied by the image's resolution to acquire S_{obs} (in metres). This measurement of S_{obs} is taken at every pixel along the shadow's length (i.e. the axis perpendicular to the Sun's line of sight) in order to produce a profile of the shadow width.

However, if any bright features are found, as per the method in Section 3.1.4, then the aligned binary shadow mask requires further treatment before measuring S_{obs}. For those bright features that are found to be closer to the pit's rim than the shadow's edge, then all shadow pixels between them and the rim along the Sun's line of sight are removed. This effectively means that the calculated apparent depth is now the relative depth from the bright feature to the shadow's edge.

Alternatively, if the feature is closer to the shadow's edge than the pit's rim, then all shadow pixels beyond it are removed, meaning the apparent depth is now the relative depth from the rim to the bright feature. Due to the risk that detected bright features are only artefacts of the image, or caused by reflection of a sunlit object elsewhere in the pit, S_{obs} is also measured upon a shadow mask where all holes are filled. This provides a range of possible values to display within the apparent depth profiles.

3.2.2 *Correcting shadow widths for non-nadir observations*

As mentioned in Section 1, Cushing et al. (2015) apply a correction factor to the manual shadow width measurements made within all HiRISE images with an emission angle (ε) greater than 5°. ε is the angle between the satellite and a normal drawn from the surface, and is shown in Fig. 6. The satellite will also have an azimuth angle (ω), which is the clockwise angle between the same reference point as for φ and the point directly below the satellite (see Fig. 5). As discussed in Section 5, ε plays an important role in correctly calculating h since the camera will observe a distorted shadow within any image where ε is non-zero.

The motivation for applying a 'ε-correction' is that when the HiRISE camera is pointing in the same direction as the Sun's illumination, it will observe a foreshortened shadow due to the pit's rim partially obscuring its view. Whereas the shadow will appear enlarged when HiRISE and the Sun are looking in opposite directions as some of the shadowed pit wall will now be visible. The scale of these distortion effects will depend on the degree of ε (see Cushing et al. 2015, fig. 9).

In their correction, Cushing et al. (2015) assume that the Sun and the HiRISE camera are always pointing either due east or west (i.e. φ and ω must equal 90° or 270°). This may be suitable for HiRISE imagery at non-polar latitudes, but this may not be the case for all spacecraft in orbit around Mars or other planetary bodies. Therefore, in this work we present a generalization of this correction method such that it can be employed for all values of φ, ω, and ε.

The aim is to retrieve the true shadow width (S_{true}) that would be observed if ε was zero. This is achieved by calculating the obliquity of the satellite parallel and perpendicular to the Sun's line of sight ($\varepsilon_{\parallel}$ and $\varepsilon_{\perp}$, respectively, and shown in Fig. 6). The purpose for calculating these separate variables is that a non-zero $\varepsilon_{\parallel}$ will lead to a distorted shadow width measurement, and ultimately an incorrect h value. Whereas a non-zero $\varepsilon_{\perp}$ will cause an incorrect shadow length measurement. In order to get an accurate S_{true}, the ε-correction presented in this section adapts the equations presented in Cushing et al. (2015) by replacing ε for $\varepsilon_{\parallel}$.

The first step in deriving $\varepsilon_{\parallel}$ and $\varepsilon_{\perp}$ is to calculate the ground distance (in metres) between the centre of the image and the satellite (d_g) using equation (11), where d_s is the slant distance (in metres) between the satellite and the centre of the image. d_s is also provided in the PDS3 index file. Any 'ground' distances referred to in this section are taken parallel to the horizon, rather than along the surface as it curves beyond it.

$$d_g = d_s \cdot \sin \varepsilon. \tag{11}$$

d_s is also used in equation (12) for finding the satellite's altitude above the horizon (d_h).

$$d_h = d_s \cdot \cos \varepsilon. \tag{12}$$

Fig. 6 shows how the parallel ground distance from the subsatellite point to the centre of the image (v) and the perpendicular ground distance from the subsatellite point to the Sun's line of sight (u) can be calculated using equations (13) and (14).

$$v = d_g \cdot |\cos \gamma|, \tag{13}$$

$$u = d_g \cdot \sin \gamma, \tag{14}$$

where γ is the ground phase angle between Sun and satellite, which is defined as the smallest absolute difference between φ and ω, meaning that γ can range between 0° and 180°.

Therefore, Fig. 6 shows how $\varepsilon_{\parallel}$ and $\varepsilon_{\perp}$ can now be found using equations (15) and (16), respectively.

$$\varepsilon_{\parallel} = \arctan\left(v/d_h\right), \tag{15}$$

$$\varepsilon_{\perp} = \arctan\left(u/d_h\right). \tag{16}$$

In case (A) where $0° \leq \gamma < 90°$ (i.e. the Sun and the satellite are pointing roughly in the same directions), we can correct S_{obs} to find S_{true} using equation (17), which has been adapted from equations (3) to (5) of Cushing et al. (2015).

$$S_{\text{true}} = S_{\text{vis}} + \frac{S_{\text{vis}} \cdot \tan \varepsilon_{\parallel}}{\tan \alpha - \tan \varepsilon_{\parallel}}, \tag{17}$$

where the solar incidence angle (α) is defined as the angle between the Sun and a normal drawn from the surface and S_{vis} is the true width of the visible portion of the shadow not blocked from view of the satellite by the pit's rim. S_{vis} is given by equation (18).

$$S_{\text{vis}} = \frac{S_{\text{obs}}}{\cos \varepsilon_{\parallel}}. \tag{18}$$

Meanwhile, in case (B) where $90° < \gamma \leq 180°$ (i.e. the Sun and satellite are pointing in approximately opposite directions to one another), S_{true} is found using equation (19), which has been adapted from equations (7) to (9) of Cushing et al. (2015).

$$S_{\text{true}} = \frac{S_{\text{obs}} \cdot \sin \alpha}{\cos\left(90° - \alpha - \varepsilon_{\parallel}\right)}. \tag{19}$$

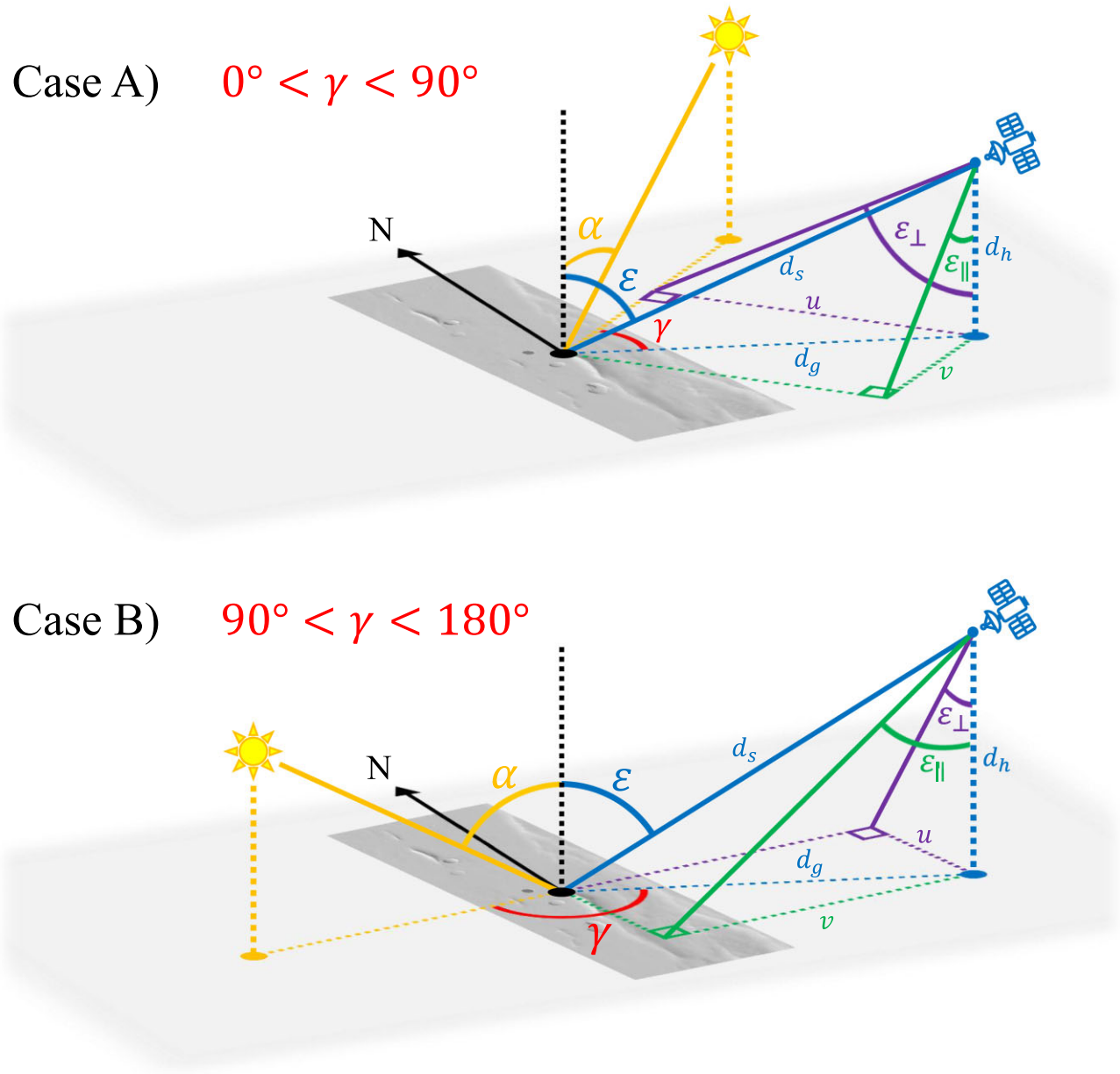

Figure 6. Schematic (overlaid on HiRISE image ESP_011531_2065_RED) of the sensing parameters in two examples of the cases (A) and (B) where the satellite and Sun are pointing in approximately the same or opposite directions (i.e. $0^\circ \leq \gamma < 90^\circ$ or $90^\circ < \gamma \leq 180^\circ$, respectively). Each of these parameters are defined in Section 3.2.2. Cases (A) and (B) dictate how the shadow width observed by the satellite (S_{obs}) is corrected to obtain the true shadow width (S_{true}) as if the emission angle (ε) was zero. The black, yellow, and blue dots represent the image centre, and the subsolar and subsatellite points, respectively.

Otherwise, in the event that $\gamma = 90^\circ$, $\varepsilon_\parallel$ will be zero, meaning that there will be no distortion in the observed shadow width (i.e. $S_{true} = S_{obs}$). While $\gamma \neq 0$ or 180°, a correction can also be applied to the observed length of the detected shadow (L_{obs}) using equation (20) to retrieve the true shadow length (L_{true}). L_{obs} is simply the length of the detected shadow (in pixels) multiplied by the image's resolution (in m per pixel). Correcting L_{obs} does not affect the h profile directly, but rather serves as a reference for where the profile is taken along the length of the pit.

$$L_{true} = \frac{L_{obs}}{\cos \varepsilon_\perp}. \quad (20)$$

When this ε-correction was applied to all 123 HiRISE images used in this work, the difference between the h values (the derivation of which is detailed in the Section 3.2.3) before and after ε-correction was found to be ≈ 14.5 per cent on average and ≈ 231.4 per cent at its maximum (when $\varepsilon_\parallel = 28.9^\circ$).

3.2.3 *Calculating apparent depth profiles*

Since S_{obs} has been automatically measured and corrected for non-nadir observations to obtain S_{true}, the apparent depth (h) can now be found. Fig. 7 takes a cross-section of a simplified pit along the Sun's line of sight, showing how a value for S_{true} can be combined with knowledge of α (also retrieved from the PDS3 index file) to calculate

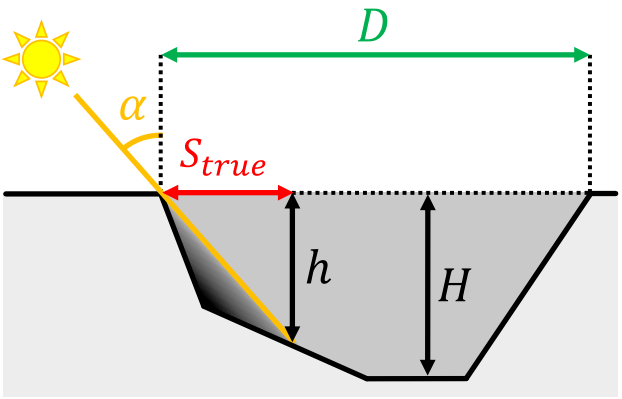

Figure 7. The cross-section of a simplified pit with an uneven floor as taken along the Sun's line of sight. This figure shows how the apparent depth (h) can be found using the solar incidence angle (α) and the true shadow width (S_{true}). The diameter (D) is not measured by PITS. Instead, the tool focuses on producing a profile for h along the entire length of the shadow, instead of calculating the maximum depth (H) like Wyrick et al. (2004), since this requires the assumption that all pits are conical in volume.

h using equation (21) (adapted from the equation used by Wyrick et al. 2004).

$$h = S_{\text{true}} \cdot \tan\alpha. \tag{21}$$

Unlike Wyrick et al. (2004), PITS does not assume that all pits are conical, since this was visibly untrue for the majority of the APC features observed in this work. Moreover, no suitably robust method of automatically measuring the diameter (D) could be found, which is necessary for deriving the maximum depth (H). Instead, the tool focuses on extracting the full shadow using image segmentation such that S_{true} can be measured at every pixel along the entire length of the shadow – rather than just at one location. This means that a profile of h is produced, whereas previously h has been provided as a single value (Wyrick et al. 2004; Cushing et al. 2015). This h profile is built up of the relative depths between the pit's rim and the shadow's edge along the Sun's line of sight, taken at each pixel in the shadow's length.

It should be noted that regions of PITS' h profiles that correspond to where the shadow's edge is adjacent to the pit wall/rim, should be treated as a minimum depth since the full width could not be measured. This is particularly relevant for deep features whose floors are completely covered in shadow. An example of the h profile produced by PITS for the HiRISE image ESP_066942_1735_RED of MGC^3 feature APC015 can be found Fig. 8.

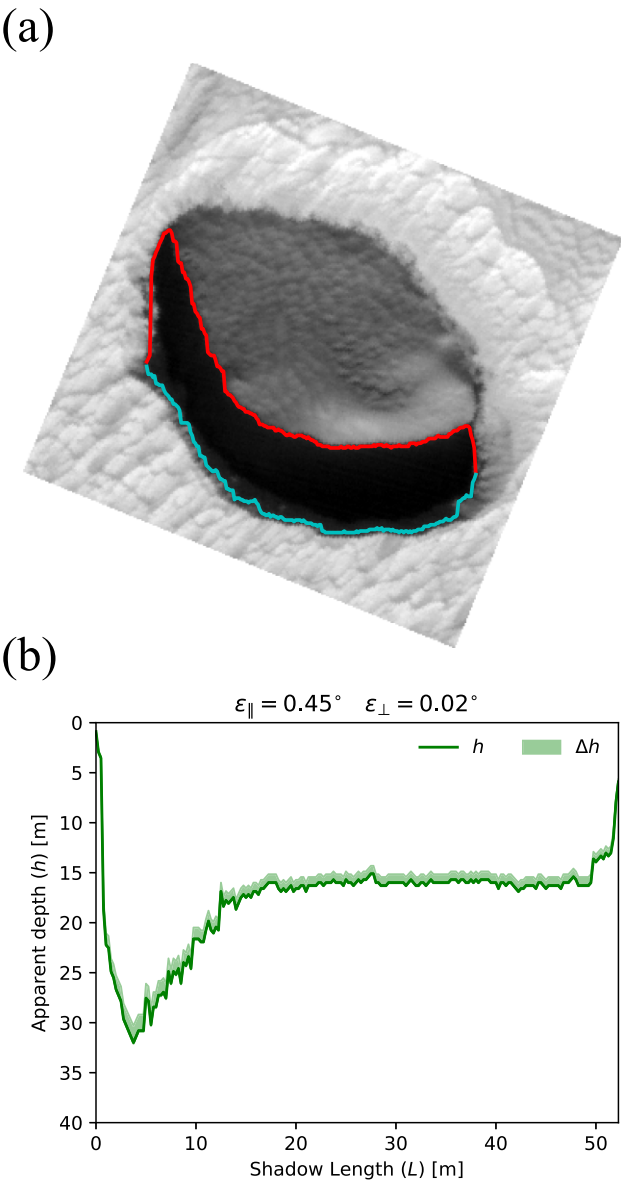

Figure 8. (a) Shows the MGC^3 feature APC015 as seen in HiRISE image ESP_066942_1735_RED. The image has been rotated using the solar azimuth angle (φ) so that the Sun's line of sight now passes from bottom to top in the image. The red and blue lines correspond to the pit's rim and the shadow's edge, respectively, which were automatically detected by PITS. (b) Gives the apparent depth (h) profile calculated by PITS upon (a). This profile represents the relative depth between the rim and the shadow's edge shown in (a).

3.3 Error analysis

As can be seen from equation (21) for finding h along the length of the shadow, as well as equations (17) and (19) for deriving S_{true}, the uncertainty in h (Δh) ultimately depends on a variety of factors.

The first step towards finding Δh is determining the uncertainty in S_{true} (ΔS_{true}), which itself depends on the uncertainties in S_{obs}, ε, and α (ΔS_{obs}, $\Delta\varepsilon$, and $\Delta\alpha$). The values for ε and α, which are given within the PDS3 index files, are taken at the centre of the HiRISE image. Therefore, there will be an uncertainty in these values when using them to calculate h, since the pit could fall anywhere within the minimum and maximum latitude/longitude coordinates of the image. However, due to the significant distance between the Sun and Mars, $\Delta\alpha$ was found to be negligible. Even for the HiRISE image with the largest footprint (of those described in Section 2), $\Delta\alpha$ represented only 1×10^{-5} per cent of the value for α.

Whilst $\Delta\alpha$ may be negligible, the altitudes of planetary remote-sensing cameras render $\Delta\varepsilon$ too significant to ignore. Thanks to the PDS3 index files, both the range of latitude/longitude coordinates of the image and the distance between the camera and the image centre are known for every HiRISE RDRV11 product. PITS is then able to use these values to calculate the maximum and minimum possible values for ε for each image to use as $\Delta\varepsilon$. A maximum value of $\Delta\varepsilon = 0.063^{\circ}$ was calculated across all 123 HiRISE images. As a result, $\Delta\varepsilon$ can become relatively high compared to ε when the satellite is very close to looking through nadir.

Table 1. Average performance scores of shadow pixel detections with Otsu's method and *k*-means clustering with silhouette analysis across 19 shadow-labelled HiRISE red-band images of MGC^3 APCs. The table compares the average precision $(\bar{\mathrm{P}})$, recall $(\bar{\mathrm{R}})$, and F1 scores $(\bar{\mathrm{F1}})$ of each method, with the maximum of each score highlighted in bold. For *k*-means clustering with silhouette analysis, the results of using the *k* values which maximized the overall silhouette score, and the silhouette coefficient of the darkest cluster ($\bar{s_0}$), are given separately. The standard deviations (SD) of each performance score across all images are given in brackets, with the minimum SD of each score across all methods also highlighted in bold.

Method	$\bar{\mathrm{P}}$ [per cent]	$\bar{\mathrm{R}}$ [per cent]	$\bar{\mathrm{F1}}$ [per cent]
Otsu's method	76.8 (22.1)	**100.0 (0.0)**	84.6 (18.4)
Silhouette score	**97.7 (2.2)**	93.4 (10.0)	95.1 (5.4)
$\bar{s_0}$	94.8 (4.2)	99.6 (1.1)	**97.1 (2.6)**

Since PITS measures a shadow's width via automated means, this will contribute an uncertainty to S_{obs} which needs to be accounted for. This uncertainty will be a factor of the expected proportion of true shadow pixels that are missed, as well as the expected rate at which non-shadow pixels are incorrectly classified as shadow. This expected uncertainty has been estimated by taking the precision and recall shadow extraction performances calculated in Section 3.1.5 and averaging them across all 19 testing images. The PSF of the HiRISE camera, which is typically only 2 pixels wide at full width at half-maximum (McEwen et al. 2007), is expected to be negligible compared to this uncertainty.

As a result of potentially different average precision and recall rates ($\bar{\mathrm{P}}$ and $\bar{\mathrm{R}}$, respectively), the upper and lower limits of ΔS_{obs} are not necessarily equal. The upper limit ($\Delta S_{\mathrm{obs},+}$) is a function of the average ratio of missed shadow pixels to all true shadow pixels (called the 'miss rate') and is equal to $1-\bar{\mathrm{R}}$. Therefore, $\Delta S_{\mathrm{obs},+}$ can be found by using equation (22).

$$\Delta S_{\mathrm{obs},+} = (1-\bar{\mathrm{R}}) \cdot S_{\mathrm{obs}}. \tag{22}$$

The lower bound $\Delta S_{\mathrm{obs},-}$ is a function of the ratio of falsely detected shadow pixels to all shadow detections (called the 'false discovery rate') and is equal to $(1-\bar{\mathrm{P}})$. $\Delta S_{\mathrm{obs},-}$ is found using equation (23).

$$\Delta S_{\mathrm{obs},-} = (1-\bar{\mathrm{P}}) \cdot S_{\mathrm{obs}}. \tag{23}$$

Now that ΔS_{obs} and $\Delta\varepsilon$ are known, ΔS_{true} can be calculated using the procedure given in Section A. This requires deriving the uncertainty in $\varepsilon_{\parallel}$ ($\Delta\varepsilon_{\parallel}$) in situations where γ does not equal 0°, 90°, or 180°. Since $\Delta\alpha$ is negligible, as mentioned previously, the uncertainty in h (Δh) is simply a function of ΔS_{true} and is given by equation (24).

$$\Delta h = \Delta S_{\mathrm{true}} \cdot \tan\alpha. \tag{24}$$

4 RESULTS

4.1 Testing shadow extraction on HiRISE imagery

4.1.1 Shadow extraction performance on red-band imagery

Table 1 presents the average precision $(\bar{\mathrm{P}})$, recall $(\bar{\mathrm{R}})$, and F1 score $(\bar{\mathrm{F1}})$ of shadow pixel detections when applying Otsu's method and *k*-means clustering with silhouette analysis to automatically extract shadows from 19 shadow-labelled HiRISE red-band images of MGC^3 APCs. Results are given separately according to whether the *k*-means algorithm has been applied using the *k* values which maximized the overall silhouette score or $\bar{s_0}$.

As Table 1 shows, extracting shadows by thresholding with Otsu's method resulted in an $\bar{\mathrm{F1}}$ of 84.6 per cent. While this may suggest high performance, this corresponds to a $\bar{\mathrm{R}}$ and $\bar{\mathrm{P}}$ of ≈ 100 per cent and 76.8 per cent, respectively. This means that the vast majority of true shadow pixels will be detected, but roughly a quarter of all shadow detections will be false. Fig. 9 displays examples of the shadows that were extracted by each method presented in Section 3.1 during testing on labelled HiRISE red-band imagery. As shown in Fig. 9, the threshold generated by Otsu's method for ESP_030995_1610_RED is clearly too weak due to the large number of FP detections. This is due to the image having a higher proportion of dark non-shadow pixels, as images with similar shading conditions were found to generate the lowest *P* across all testing images.

Table 1 also proves that, upon shadow-labelled red-band imagery, using *k*-means clustering with the *k* values which maximized $\bar{s_0}$ achieved the highest $\bar{\mathrm{F1}}$ (97.1 per cent) and $\bar{\mathrm{R}}$ (99.6 per cent). The F1 scores achieved by *k*-means clustering when maximizing $\bar{s_0}$ across all 19 red-band testing images, also possessed the lowest standard deviation (SD). However, the highest $\bar{\mathrm{P}}$ (97.7 per cent) was achieved by *k*-means clustering when the overall silhouette score was maximized.

Using *k*-means clustering with the target *k* values discussed in Section 3.1.5 upon the 19 shadow-labelled HiRISE red-band images produced an $\bar{\mathrm{F1}}$ of 98.1 per cent with a SD of 2.2 per cent, which is not significantly higher than the $\bar{\mathrm{F1}}$ in Table 1 achieved by both approaches to *k*-means clustering with silhouette analysis. As a result, silhouette analysis can be said to be a suitable method for *k* suggestion when using *k*-means clustering for automated shadow extraction.

4.1.2 Shadow extraction performance on colour imagery

PITS' automated shadow extraction has also been tested upon HiRISE colour imagery of Martian pits to determine if more image bands will lead to more accurate shadow pixel detections. Table 2 shows the $\bar{\mathrm{P}}$, $\bar{\mathrm{R}}$, and $\bar{\mathrm{F1}}$ when applying Otsu's method and *k*-means clustering with silhouette analysis across 12 shadow-labelled HiRISE colour images of MGC^3 APCs. This confirms that applying *k*-means clustering with the *k* which maximized $\bar{s_0}$ achieved the highest and least variable $\bar{\mathrm{F1}}$ across both red-band and colour images.

Since only 12 colour versions could be acquired for the 19 red-band images, the average performance scores in Tables 1 and 2 cannot be directly compared. Instead, the average performance scores for all shadow pixel detections were calculated for the 12 HiRISE red-band images that had corresponding colour versions. Otsu's method achieved an $\bar{\mathrm{F1}}$ of 79.4 per cent (with a SD of 21.1 per cent) upon these 12 red-band images. Whereas *k*-means clustering with the *k* suggested by maximizing the silhouette score or $\bar{s_0}$ achieved $\bar{\mathrm{F1}}$ values of 93.2 and 94.9 per cent (with SD of 7.2 and 4.1 per cent), respectively. Comparing these scores with those in Table 2 shows that using HiRISE colour imagery only yielded a marginal improvement in shadow extraction performance when using *k*-means clustering, but not when using Otsu's method. HiRISE colour images will have three times the number of pixels as a red version, since it has three bands as opposed to just one. Consequently, the average run-time when using colour imagery was found to be approximately three times longer than when using red-band versions.

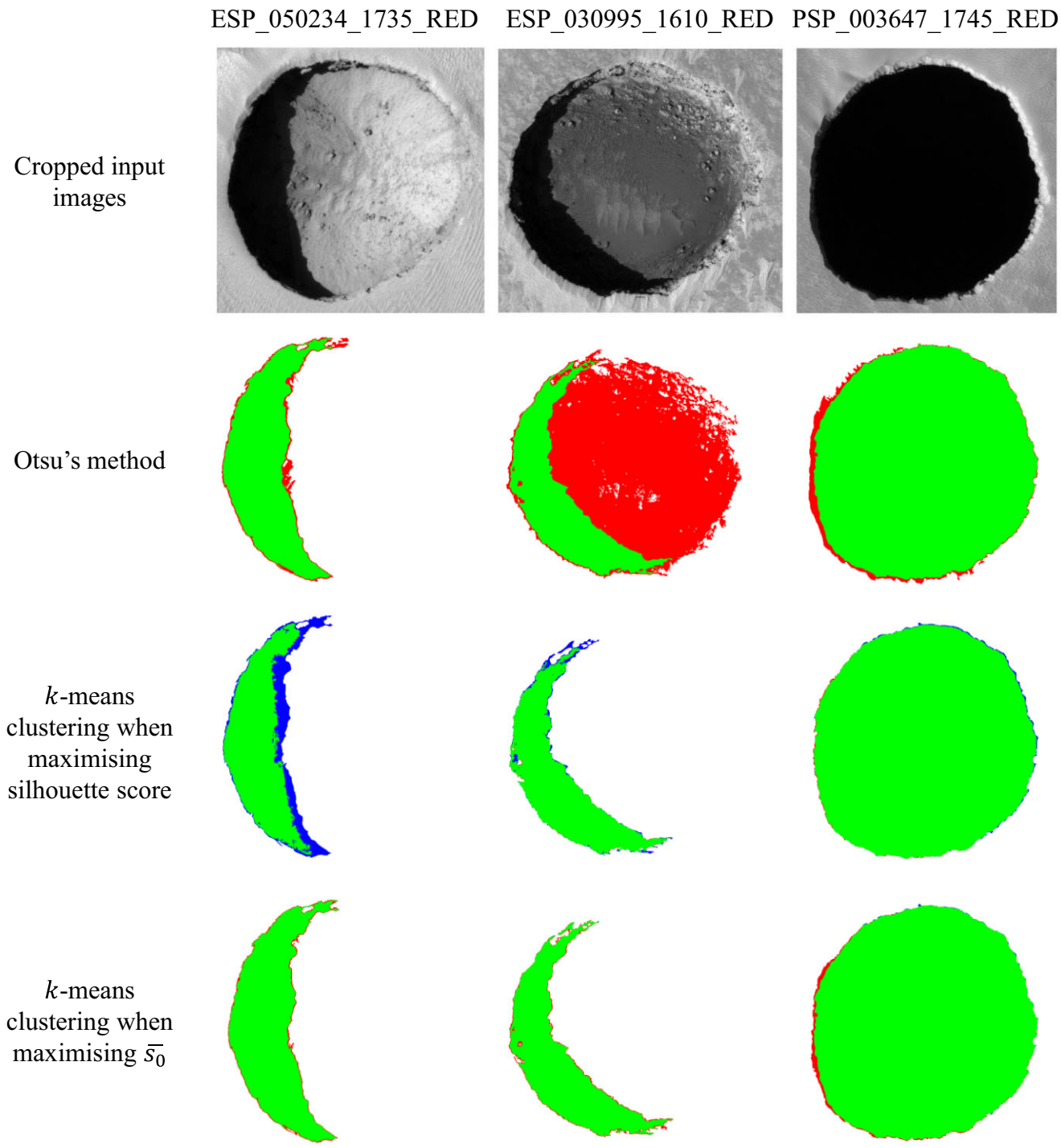

Figure 9. Examples of the shadow pixel detections using each of the methods described in Section 3.1. The example results shown here are for the HiRISE images ESP_050234_1735_RED, ESP_030995_1610_RED, and PSP_003647_1745_RED. These images were labelled, as described in Section 2, for their respective shadows to be able to assess the validity of the detected shadow pixels. The detections and omissions of each extracted shadow have been colour-coded: true positives are green, false positives are red, false negatives are blue, and true negatives have been blended into the white background.

4.2 Applying PITS to HiRISE imagery of MGC^3 APCs

As previously mentioned in Section 2, all HiRISE RDRV11 red-band images which fully contained MGC^3 APCs that exhibited shadows were acquired. PITS was then applied to these 123 HiRISE observations of 88 APCs to automatically calculate their h profiles. Due to it achieving the highest $\bar{F}1$ during testing, as detailed in Section 4.1, k-means clustering when maximizing $\bar{s_0}$ was the chosen method of automated shadow extraction. A CSV file containing the results for all 123 images can be found in the online supporting material. In order to reduce the h profiles to singular values, the h at the shadow's centre (h_c) and the maximum h (h_m) were both extracted. The file also includes the corresponding MGC^3 APC codes, HiRISE product names, image resolutions, and sensing information. Table 3

Table 2. Average performance scores of shadow pixel detections with Otsu's method and *k*-means clustering with silhouette analysis across 12 shadow-labelled HiRISE colour images of MGC^3 APCs. This table follows the same format and notation as in Table 1.

Method	$\bar{P}$ [per cent]	$\bar{R}$ [per cent]	$\bar{F1}$ [per cent]
Otsu's method	69.4 (24.6)	**100.0 (0.0)**	78.9 (21.1)
Silhouette score	92.6 (11.0)	98.9 (3.0)	95.2 (7.0)
$\bar{s_0}$	**94.1 (3.8)**	99.4 (1.4)	**96.6 (2.5)**

gives a sample of these results for the first five HiRISE images when sorted alpha-numerically by the product name.

Applying PITS to HiRISE imagery of MGC^3 APCs has also allowed the recording of the run-time, in order to suggest to a future user the approximate speed at which the tool can analyse their data set. It was found that across the full data set of 123 HiRISE images, the tool exhibited a minimum and maximum of $\approx$5 s and 500 s for images with approximately 0.02 and 4.80 Mpx, respectively. This was achieved using a laptop with an 11th generation Intel Core i5 processor and 8 GB of RAM.

4.2.1 *Investigating apparent depth variation*

Of these 88 APCs, 25 APCs were contained in one or more HiRISE RDRV11 images. This allowed for an investigation into the effect of non-zero ε values on the h values that are calculated. This was made possible by replacing S_{obs} for S_{true} in equation (21) to get the h that would be observed before applying any ε-correction (h_{obs}). As before, h_c and h_m were also recorded from the h_{obs} profile, in order to compare the variation in h profiles derived upon HiRISE images containing the same MGC^3 features before and after ε-correction. The expectation being that APCs with multiple HiRISE observations having high variation in their ε, but little variation in the Sun's position (i.e. α and φ), will also experience high degrees of variation in the h values that are calculated.

Fig. 10 compares the relative SD in the h_c values that are calculated for the 25 APCs with multiple HiRISE observations ($\sigma_h/\bar{h}$) before and after ε-correction. $\sigma_h/\bar{h}$ is the SD in the h_c values divided by their average, which avoids only larger APCs appearing to have high variation in h_c. Fig. 10 shows that before correction, $\sigma_h/\bar{h}$ reached as high as $\approx$37 per cent for some MGC^3 APCs. Whereas after correction, it can be seen that in the majority of cases, $\sigma_h/\bar{h}$ has now been significantly reduced (denoted by a green line). Despite this, $\sigma_h/\bar{h}$ in fact increases (denoted by a red line) for six APCs. The explanations for this are given in Section 5. The same trends for each APC was also seen when plotting the relative SD in the h_m values before and after correction.

4.2.2 *Comparing PITS and MGC^3 apparent depths*

As previously discussed in Section 1, it is not possible to validate the h profiles derived by PITS upon all 123 HiRISE images of 88 MGC^3 APCs due to insufficient coverage of high-resolution elevation data. Even in the few instances where such data are available, it is difficult to know exactly which pixels in an orthorectified DEM the h profile would correspond to. However, the h profiles derived by PITS can be corroborated with the manually produced h measurements made for each APC in the MGC^3 data base (Cushing 2015).

Fig. 11 compares (on a logarithmic scale) the ε-corrected h_c and h_m values calculated automatically by PITS with the MGC^3 h values for the HiRISE RDRV11 images, which were the only such observation of that MGC^3 APC. This is to ensure that the same shadow is being extracted by PITS as was measured manually by MGC^3 (i.e. so that the depth is taken at the same place within the pit). This reasoning is explained further in Section 5. If the PITS and MGC^3 h values are all equal, then they are expected to fall on the black dashed line. Fig. 11 shows that this happens on a number of occasions when plotting both h_c and h_m. However, the h_c and h_m calculated by PITS are less than the MGC^3 h for the majority of images. In fact, there are four APCs (APC001, APC029, APC048, and APC135) for which there is more than a 200 per cent difference between the MGC^3 h and both of the PITS h_c and h_m values. Possible causes are discussed in Section 5.

4.2.3 *Possible cave entrances suggested by PITS*

In applying PITS to the 123 HiRISE RDRV11 images containing 88 MGC^3 APCs, the results of 11 images suggest the possible presence of a cave entrance. Since two of the 11 images contained the same feature, this resulted in 10 APCs which could be considered as potential targets for the exploration of cave entrances. These features were identified according to three factors: the suggested presence of overhanging rims, the shape of their h profiles, and the wider context provided by the input image. Fig. 8(a) is an example of one of the 10 MGC^3 APCs considered as a potential cave entrance in this work. The image has been aligned such that the Sun's line of sight passes from bottom to top. Overlaid upon the image is the shadow edge and pit rim detected by PITS, which serves as a reference for where S_{obs} has been measured between.

First, the georeferenced shapefile containing the main shadow detected by PITS was used to crop the input HiRISE image to the shadow's perimeter. This allowed for the contrast of the pixels within the shadow to be enhanced in order to look for deeper shading indicating steep or overhanging rims, while still retaining the context of the surrounding image. A similar process has been used to produce fig. 7 of Cushing et al. (2015). Further justification for an overhanging rim is if no pit wall is visible in the image and there is a notable difference in albedo and morphology between the pit's floor and the surrounding surface. Fig. 12 displays the contrast-enhanced shadow for the same HiRISE image shown in Fig. 8.

If the contrast-enhanced shadow and/or input image suggest the presence of an overhanging rim, the APC remains in consideration if their h profile showed a gradual or sudden decline towards the suggested location of the overhanging rim. The input image is examined again to ensure that this feature of the h profile is not simply a product of an uneven pit rim casting a wider or thinner shadow. Fig. 8(b) gives an example of a h profile with a sudden decline towards a suggested overhanging rim. The near-zero $\varepsilon_\perp$ (0.02°) and the decline to the left of the h profile of approximately 15 m suggests a potential cave entrance. If $\varepsilon_\perp$ was high, then the satellite may be peering below an overhanging rim, which is casting its own shadow directly beneath.

5 DISCUSSION

What is clear from the high variability of Otsu's method when used for automated shadow extraction is that the number of clear, visibly distinct regions in satellite images of pits can vary. Different illumination conditions, surface materials, and morphologies mean that two classes are often insufficient to appropriately extract a pit's shadow. Therefore, a method of shadow extraction was required that could automatically adapt the number of classes that it would segment images into. *k*-means clustering with silhouette analysis was

Table 3. Sample of the table (available through the online supporting material in CSV format) containing the calculated h values after ε-correction for the first five HiRISE images when sorted alpha-numerically by the product name. Each images' resolution, solar incidence angle (α), solar azimuth angle (φ) and satellite emission angle (ε), and satellite azimuth angle (ω) are also given. The h values taken at the h profile's centre (h_c) and maximum (h_m) are presented separately. The corresponding upper and lower bounds of the uncertainty in h (Δh) are given first and last in brackets, respectively.

HiRISE product name	MGC^3 name	Resolution [m]	α [deg]	φ [deg]	ε [deg]	ω [deg]	h_c (+ / −) [m]	h_m (+ / −) [m]
ESP_011386_2065_RED	APC095	0.25	61.01	162.78	6.72	265.28	175.32 (0.75 / 9.17)	177.55 (0.76 / 9.29)
ESP_011531_2065_RED	APC095	0.25	61.40	159.40	8.95	82.82	176.41 (0.76 / 9.22)	177.94 (0.76 / 9.30)
ESP_011677_1655_RED	APC079	0.5	58.18	180.91	9.48	262.61	69.74 (0.30 / 3.65)	85.86 (0.37 / 4.50)
ESP_011756_1735_RED	APC091	0.25	55.56	174.52	22.18	83.13	131.52 (0.56 / 6.88)	132.10 (0.57 / 6.91)
ESP_012600_1655_RED	APC079	0.5	49.90	163.77	3.71	84.50	56.45 (0.24 / 2.95)	75.66 (0.32 / 3.96)

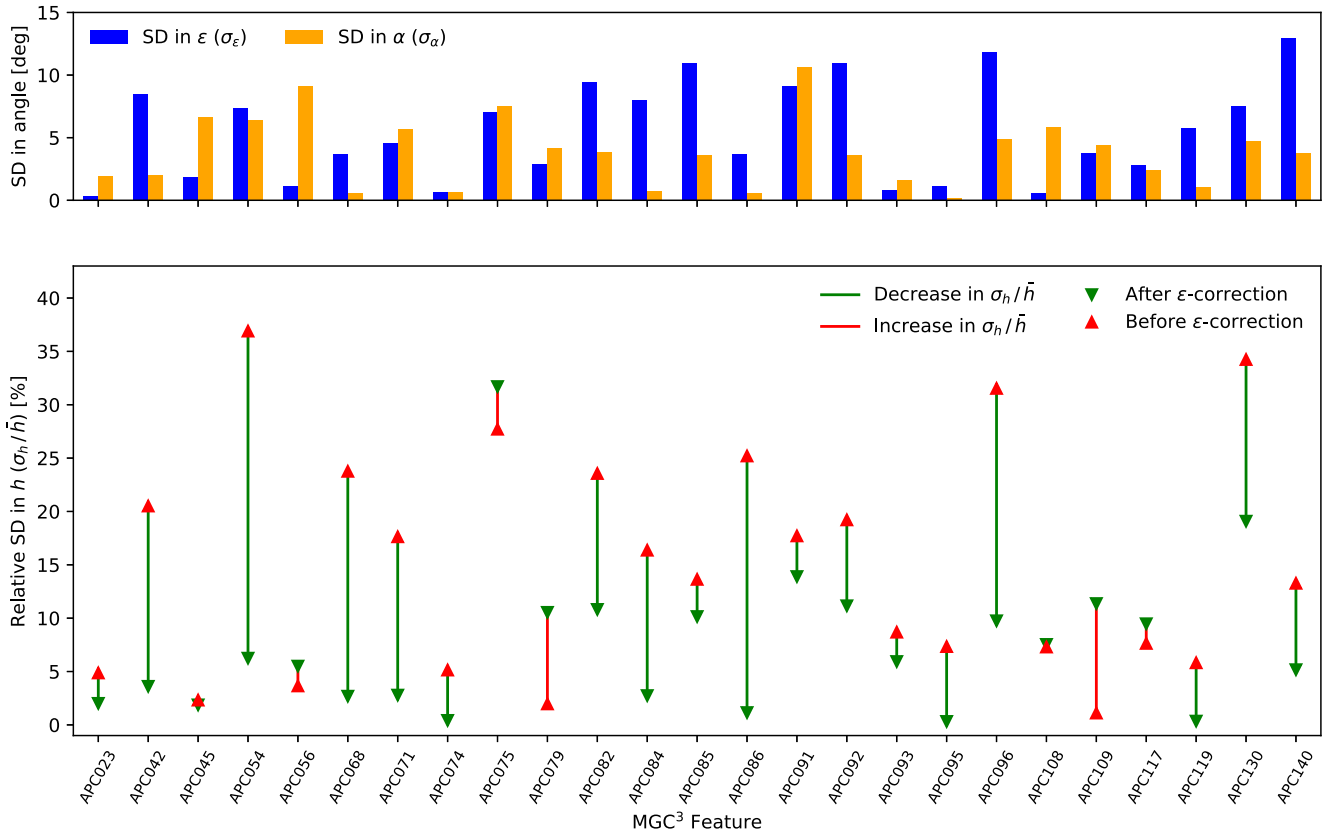

Figure 10. Comparison of the relative standard deviations (SD) in the centre apparent depth values (h_c) calculated by PITS upon multiple images taken of the same MGC^3 APC ($\sigma_h/\bar{h}$) before and after correcting for non-zero ε values. The $\sigma_h/\bar{h}$ before correction is represented by a red, upwards triangle. Whereas the $\sigma_h/\bar{h}$ after correction are given as green, downwards triangle. Similarly, scenarios where $\sigma_h/\bar{h}$ has increased or decreased after correction for a particular APC are denoted by a red or green line, respectively. It can be seen that correcting for non-zero ε values has significantly reduced the $\sigma_h/\bar{h}$ in the majority of APCs with multiple HiRISE observations. However, $\sigma_h/\bar{h}$ has in fact increased (to varying degrees) for the features: APC056, APC075, APC079, APC108, APC109, and APC117. Although, reasons for this are outlined in Section 5, the SD in the images' emission (σ_ε) and incidence (σ_α) angles are also given for context about possible causes of high $\sigma_h/\bar{h}$.

the preferred option since its objective is similar to the definition of a shadow (uniformly dark, but also distinct from its surrounding). It was expected that maximizing $\bar{s_0}$ would achieve the highest $\bar{\text{F1}}$ across the shadow-labelled red-band and colour HiRISE imagery, since PITS classifies the darkest cluster as the shadow, meaning that it was critical for this cluster to be as appropriate as possible. For example, it is possible that a value of k could generate the highest overall silhouette score, without also generating the highest $\bar{s_0}$.

A small improvement in the $\bar{\text{F1}}$ was observed while using k-means clustering with silhouette analysis upon colour versus red-band imagery. However, the $\bar{\text{F1}}$ was marginally lower for colour imagery when applying Otsu's method. This suggests that the appearance of a pit's shadow is consistent across multiple HiRISE colour bands, but not all three. This is likely because Otsu's method operates on an image that is averaged across all colour bands, whilst k-means clustering assigns pixels to a cluster based on the modal cluster label across all bands. Therefore, due to the already high performance and improved run-time, it is recommended to apply PITS (which utilizes k-means clustering when maximizing $\bar{s_0}$) to red-band imagery when dealing with Martian pits imaged by HiRISE. None the less, it is possible that applying PITS to data from other sensors, or from other planetary bodies, reveals different results. As a result, the functionality of extracting pit shadows from colour imagery remains in the algorithm.

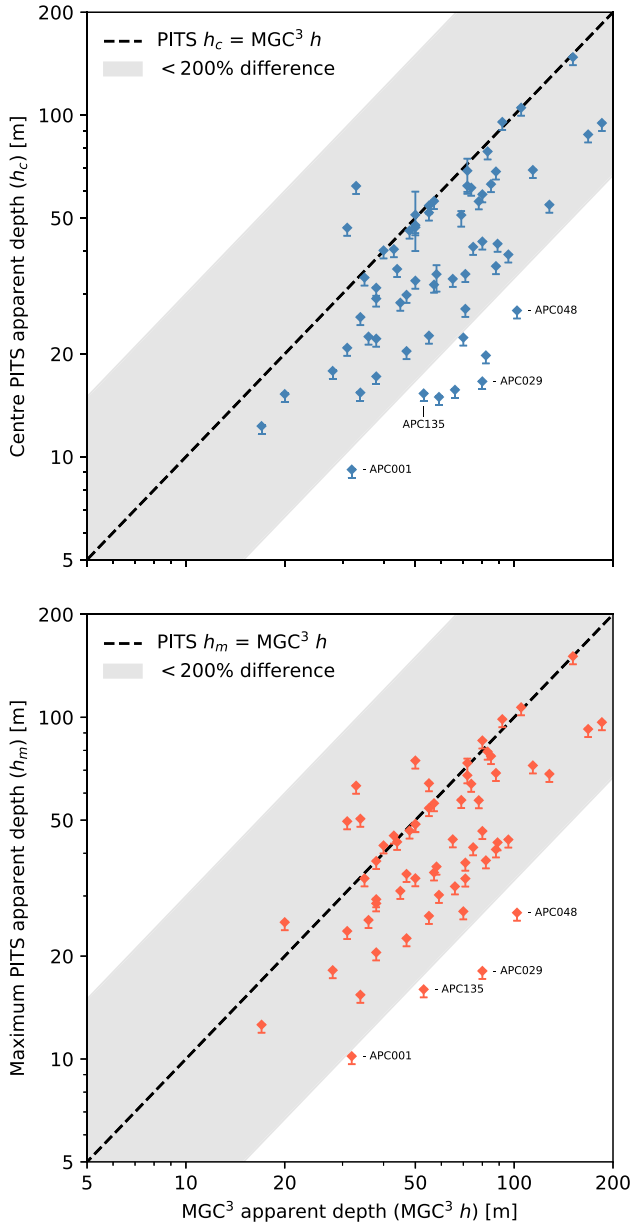

Figure 11. Apparent depths calculated by PITS compared to those in the MGC^3 catalogue for the HiRISE RDRV11 images, which were the only such observation of that MGC^3 APC. The PITS h values have been corrected for all values of ε, whereas Cushing et al. (2015) apply a correction to all images with $\varepsilon > 5°$. The top axis plots the h taken at the centre of PITS' h profile (h_c), with the bottom plotting the maximum h (h_m) from the profile. The error bars for h_c and h_m are equal to Δh, as calculated in Section 3.3. If PITS extracts a shadow from the same image as was used to produce the MGC^3 h, the expectation is that h_c and h_m should fall close to the black dashed line. However, h_c and h_m were found to both disagree with MGC^3 by more than 200 per cent for four APCs: APC001, APC029, APC048, and APC135.

Applying PITS to multiple HiRISE red-band images containing the same MGC^3 APCs revealed the influence of ε on the variation of h profiles that are calculated. Before performing any ε-correction, $\sigma_h/\bar{h}$ was regularly exceeding 20 per cent in Fig. 10. This can be caused by either the Sun or the satellite's position in the sky varying significantly. Varying values of α and/or φ will result in the shadow's edge being cast into a different location of the pit floor, which can cause a different h that is calculated for APCs with uneven floors or

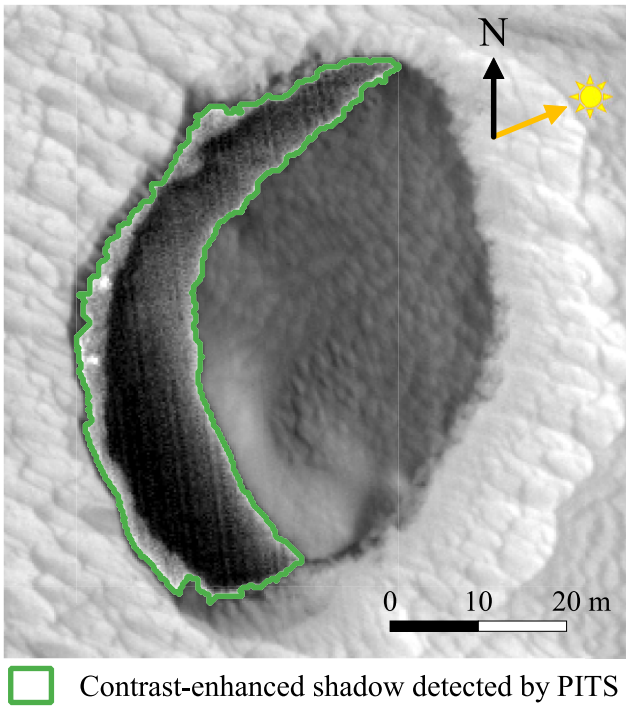

Figure 12. Contrast-enhanced shadow suggesting possible overhanging rims overlaid on the HiRISE image ESP_066942_1735_RED, which itself contains the MGC^3 feature APC015. This is the same image as the one shown in Fig. 8, with the directions of north and the Sun's line of sight given for reference. The contrast of the shadow pixels was enhanced by cropping the HiRISE image to the extents of the shadow using the georeferenced shadow shapefile automatically extracted by PITS.

rims. High variation in h is also due to these multiple images of the same APC having a larger range of ε. This is supported by the fact that the $\sigma_h/\bar{h}$ that was calculated after ε-correction was very low for images of the same APC that also had a low σ_α. In essence, the Sun's position has not significantly changed, so the corrected h values are now consistent.

The significant decreases in $\sigma_h/\bar{h}$ prove the need for correcting shadow widths measured from satellite imagery. However, $\sigma_h/\bar{h}$ was seen to increase for six APCs despite ε-correction. APC075 is a sufficiently deep pit that, despite a difference in α of nearly 20° between the three HiRISE images, its floor was completely covered in shadow in every image (i.e. S_{true} did not change). As a result, the α led to a high $\sigma_h/\bar{h}$, which was then exacerbated when correcting for ε.

APC056, APC079, and APC108 were all contained within two HiRISE images each, with one of the two images having higher α and ε values than the other, and vice versa. The images taken of these features also had γ values close to 0° or 180°. This meant that while the larger α was casting a wider shadow in one image, the larger ε was making this width appear thinner. This resulted in consistent S_{obs} measurements despite the clear variation in α placing the shadow's edge at a different depth. Correcting for the change in ε then revealed the correct S_{true}, ultimately causing $\sigma_h/\bar{h}$ to increase.

For the features APC109 and APC117, there was only image for which γ was close to 180° that also had the largest ε, meaning that $S_{\text{obs}} > S_{\text{true}}$. Whereas the other image containing the two features had a smaller ε, or a γ close to 90°, meaning that the difference between S_{obs} and S_{true} was not as great in this particular image. Therefore, the $\sigma_h/\bar{h}$ increased after applying ε-correction.

A comparison between the apparent depths provided in the MGC^3 catalogue for each MGC^3 APC with those calculated by PITS has also been made in Fig. 11. While PITS and MGC^3 agree on several occasions, there is also large disagreement (of more than 200 per cent). Where this occurred for both h_c and h_m, the shadows extracted by PITS were individually inspected, which exhibited no visible errors that would cause such deviation. Manual measurements of $S_{\rm obs}$, followed by the depth calculation and ε-correction procedure in this work, yielded similar results. This was also the case when the correction procedure utilized by Cushing et al. (2015) was followed for only those images with $\varepsilon > 5^\circ$.

It can be assumed that the MGC^3 h values were produced upon the same HiRISE RDRV11 image as PITS has been applied to if it is the only such image containing that particular feature. The MGC^3 h could also have been produced from self-processed HiRISE experiment data record images which, since the publication of the MGC^3 catalogue, are now available in the RDRV11 data set. Where multiple HiRISE images contain the same feature, Cushing (2015) 'typically' chose the one with the smallest α to calculate h. Since this is not an absolute statement, multiple HiRISE observations of the same features have not been plotted. Hence, the Sun and shadow should have been in the same positions when the MGC^3 and PITS h values were produced. In addition, if the MGC^3 depths are all truly apparent depths, they should not be noticeably greater than h_m. Therefore, a likely explanation for this deviation is that occasionally the depths provided in MGC^3 are estimates of the maximum depth of the pit – perhaps similar to the procedure used by Wyrick et al. (2004). This is supported by the aforementioned statement in the MGC^3 documentation that apparent depths were 'generally' derived, and would explain why the majority of h_c and h_m values are less than the corresponding MGC^3 depths.

6 CONCLUSIONS

The PITS tool described in this work has been tested with a range of image segmentation methods in order to automatically extract shadows from remote-sensing images of pits. This is for the purpose of measuring the shadow's width along its entire length which, along with knowledge of the Sun's position, returns a profile of the pit's apparent depth (h) – the relative depth at the edge of the shadow. This is an automated approach to calculating h, which has been performed manually before in literature (Wyrick et al. 2004; Cushing et al. 2015). In this work, we have also presented a generalization of the correction applied by Cushing et al. (2015) such that PITS can accurately correct the observed shadow widths for all values of ε, φ, and ω.

Otsu's method and k-means clustering with silhouette analysis were adapted and tested for automated shadow extraction from shadow-labelled HiRISE imagery of MGC^3 APCs (19 red-band and 12 colour images in total). This found that Otsu's method generated highly variable results, since only two classes (foreground and background) were often insufficient to delineate the shadow without including non-shadow pixels within the detection. k-means clustering with silhouette analysis was also tested when maximizing the overall silhouette score of all clusters and when only maximizing the silhouette coefficient of the darkest cluster ($\bar{s_0}$). The latter achieved the highest and least variable $\bar{\rm F}1$ of 97.1 per cent (with an SD of 2.6 per cent) upon the 19 red-band images across all methods of automated shadow extraction tested in this work. Therefore, k-means clustering with silhouette analysis when maximizing $\bar{s_0}$ is the method that has been implemented into the PITS algorithm.

A marginal improvement in $\bar{\rm F}1$ was also observed when applying k-means clustering when maximizing $\bar{s_0}$ to the 12 colour images compared to the performance on the corresponding red versions. Yet, this increase was not sufficiently large to be able to warrant the significant increase in average run-time. This may not be true for data collected by other sensors or especially other bodies – perhaps where the intensity across all colour bands is more uniform. As such, PITS can still be applied to multiband imagery of pits, despite red-band imagery being the recommendation when applying the tool to HiRISE imagery.

PITS has also been applied to 123 HiRISE red-band observations of 88 MGC^3 APCs. Across the entire data set, PITS exhibited a minimum and maximum run-time of $\approx$5 and 500 s, respectively. This variation in run-time was a result of the tool being applied to a range of image sizes. These are clearly much shorter time-scales than could be achieved manually, considering the range of products that PITS can output. This also revealed that applying the ε-correction described in Section 3.2.2 significantly reduced the relative SD in the h calculated by PITS ($\sigma_h/\bar{h}$) for the majority of APCs which have multiple HiRISE observations. In the situations where $\sigma_h/\bar{h}$ did increase after ε-correction, this is explained by the shadow's edge being cast to a location in the pit floor at a different depth, or the pit's floor being fully covered in shadow over multiple images with ranging α.

Without sufficient coverage of high-resolution elevation data, the h values calculated by PITS for these 88 APCs have been compared to the depths provided in the MGC^3 catalogue. According to the relevant documentation, these MGC^3 h were 'generally' calculated using the approach in Cushing et al. (2015), with a correction being applied to all images with $\varepsilon > 5^\circ$ (Cushing 2015). Assuming that PITS and MGC^3 have measured shadow widths from the same HiRISE images, the h_c and h_m calculated by PITS upon images that are the only HiRISE RDRV11 image containing a given APC were plotted against their corresponding MGC^3 h. This showed that PITS and MGC^3 calculate comparable h in the majority of cases. Although for the features where they disagreed most, it was found that there were no visible errors with the extracted shadows. This suggests that some of the MGC^3 APC depths are instead estimates of the maximum depth of the pit, as opposed to the apparent depth. This is supported by the above statement in the MGC^3 documentation, as well as the fact that the h_c and h_m calculated by PITS are less than those in MGC^3 in the majority of instances.

The outputs upon these 123 HiRISE images have been used to identify 11 examples (taken of 10 APCs) whose h profiles, as well as the context provided by the image, suggest that they could be possible cave entrances. The wider context came in the form of using PITS' georeferenced shapefiles of the detected shadows to enhance the contrast of the shadow pixels, whereby any deeply shaded regions may be due to steep or overhanging rims. These 10 APCs were considered a possible cave entrances since their h profiles exhibited a decline towards one of these deeply shadowed regions (as shown in Figs 8 and 12). It was also considered whether wider shadows were in fact being cast by an uneven pit rim, as opposed to being a result of the pit's topography. While it is impossible to definitively confirm that these features are indeed cave entrances without exploring them on the surface, tools such as PITS will help us to narrow-down the features with the highest priority for investigating Martian cave entrances for astrobiological significance and habitability feasibility.

The approach of PITS is highly applicable to data from other sensors observing Mars, provided that pits are visible with sufficient detail within the confines of the sensor's resolution. Therefore, PITS

should be tested with the same procedure in this work upon data from the ExoMars Trace Gas Orbiter Colour and Stereo Surface Imaging System (CaSSIS; Thomas et al. 2017). PITS may also be used for satellite imagery taken in orbit around other rocky Solar System bodies – particularly the Moon. As such, preliminary results have been retrieved when applying PITS to Lunar Reconnaissance Orbiter (LRO) Narrow Angle Camera (NAC) imagery (Robinson et al. 2010) containing Lunar Pits Atlas features (Wagner & Robinson 2021), which indicate similarly high shadow detection performance. With repeat coverage of the same features being far more common with LRO NAC images compared to HiRISE, future work will also involve combining the h profiles from multiple images to derive a 3D model.

ACKNOWLEDGEMENTS

This project is part of the Europlanet 2024 RI which has received funding from the European Union's Horizon 2020 research and innovation programme under grant agreement No. 871149.

DATA AVAILABILITY

MRO HiRISE RDRV11 data (McEwan 2007) was acquired via the Mars Orbital Data Explorer (found at https://ode.rsl.wustl.edu/mars/) of NASA's Planetary Data System (PDS) Geosciences Node. The cumulative PDS3 index file for the HiRISE RDRV11 data set was also accessed from PDS (at https://hirise-pds.lpl.arizona.edu/PDS/). The Mars Global Cave Candidate Catalogue (MGC^3) was retrieved from the USGS Astropedia service (Cushing 2015). and imported into JMARS (Christensen et al. 2009) in order to convert the catalogue from CSV to ESRI shapefile format. A CSV file containing the h_c and h_m calculated by PITS upon all 123 HiRISE images of MGC^3 APCs can be found in the online supporting material. This file also includes the corresponding MGC^3 code-name, HiRISE product name, and sensing information (i.e. image resolution, α, φ, ε, and ω). The h profiles derived from the 11 HiRISE images of 10 APCs that suggest possible cave entrances are also given in the online supporting material, along with the detected shadows as georeferenced shapefiles. The PITS tool itself is publicly available through GitHub (https://github.com/dlecorre387/Pit-Topography-from-Shadows), where there is an installation guide and a user tutorial.

REFERENCES

Atri D. et al., 2022, preprint (arXiv:2208.00892)
Boston P. J., Frederick R. D., Welch S. M., Werker J., Meyer T. R., Sprungman B., Hildreth-Werker V., Thompson S. L., 2004, in El-Genk M. S., ed., AIP Conf. Proc. Vol. 699, Space Technology and Applications. Am. Inst. Phys., New York, p. 1007
Christensen P. R., Engle E., Anwar S., Dickenshied S., Noss D., Gorelick N., Weiss-Malik M., 2009, AGU Fall Meeting Abstracts, IN22A–06
Cushing G. E., 2015, Mars Global Cave Candidate Catalog PDS4 Archive Bundle, PDS Cartography and Imaging Sciences Node (IMG). Available at: https://astrogeology.usgs.gov/search/map/Mars/MarsCaveCatalog/mars_cave_catalog
Cushing G. E., Titus T. N., Wynne J. J., Christensen P. R., 2007, Geophys. Res. Lett., 34, L17201
Cushing G. E., Okubo C. H., Titus T. N., 2015, J. Geophys. Res. (Planets), 120, 1023
Davey S. C., Ernst R. E., Samson C., Grosfils E. B., 2013, Can. J. Earth Sci., 50, 109
Ferrill D. A., Morris A. P., 2003, J. Struct. Geol., 25, 183
Ferrill D. A., Hargitai H., Kereszturi Á., 2015, Pit. Springer, New York, p. 1566
Gadányi P., van der Bogert C. H., 2014, Lava Tube. Springer, New York, p. 1
Gillis-Davis J. J., Blewett D. T., Gaskell R. W., Denevi B. W., Robinson M. S., Strom R. G., Solomon S. C., Sprague A. L., 2009, Earth Planet. Sci. Lett., 285, 243
Hagen T. H., 2014, Pit Crater Chain, Pit Chain. Springer, New York, p. 1
Kirk R. L. et al., 2008, J. Geophys. Res. (Planets), 113, E00A24
Lagain A., Servis K., Benedix G. K., Norman C., Anderson S., Bland P. A., 2021, Earth Space Sci., 8, e01598
McEwan A., 2007, Mars Reconnaissance Orbiter High Resolution Imaging Science Experiment, Reduced Data Record, MRO-M-HIRISE-3-RDR-V1.1, NASA Planetary Data System
McEwen A. S. et al., 2007, J. Geophys. Res.: Planets, 112, E05S02
Mouginis-Mark P. J., Rowland S. K., 2001, Geomorphology, 37, 201
Nodjoumi G., Pozzobon R., Rossi A. P., 2021, in 52nd Lunar and Planetary Science Conference, held virtually. Lunar and Planetary Science Conference. p. 1316
Otsu N., 1979, IEEE Trans. Syst. Man Cybernet., 9, 62
QGIS Development Team, 2022, QGIS Geographic Information System, QGIS Association. Available at: https://www.qgis.org
Rajaneesh A., Vishnu C. L., Oommen T., Rajesh V. J., Sajinkumar K. S., 2022, Icarus, 376, 114886
Robinson M. S. et al., 2010, Space Sci. Rev., 150, 81
Rousseeuw P. J., 1987, J. Comput. Appl. Math., 20, 53
Sauro F., Pozzobon R., Massironi M., De Berardinis P., Santagata T., De Waele J., 2020, Earth-Sci. Rev., 209, 103288
Som S. M., Greenberg H. M., Montgomery D. R., 2008, Int. J. Mars Sci. Explor., 4, 14
Tertius Bickel V., Conway S., Tesson P.-A., Manconi A., Loew S., Mall U., 2020, IEEE J. Select. Topics Appl. Earth Obs. Remote Sens., 13, 2831
Thomas N. et al., 2017, Space Sci. Rev., 212, 1897
van der Bogert C. H., Ashley J. W., Ferrill D., 2014, Pit Crater. Springer, New York, p. 1
Wagner R. V., Robinson M. S., 2014, Icarus, 237, 52
Wagner R. V., Robinson M. S., 2021, in 52nd Lunar and Planetary Science Conference, held virtually. Lunar and Planetary Science Conference, p. 2530
Wang Y., Di K., Xin X., Wan W., 2017, ISPRS J. Photogramm. Remote Sens., 129, 12
Williams K. E., McKay C. P., Toon O. B., Head J. W., 2010, Icarus, 209, 358
Wyrick D., Ferrill D. A., Morris A. P., Colton S. L., Sims D. W., 2004, J. Geophys. Res.: Planets, 109, E06005

SUPPORTING INFORMATION

Supplementary data are available at *RASTAI* online.

Table 3. Sample of the table containing the calculated h values after ε-correction for the first five HiRISE images when sorted alpha-numerically by the product name.

Please note: Oxford University Press is not responsible for the content or functionality of any supporting materials supplied by the authors. Any queries (other than missing material) should be directed to the corresponding author for the article.

APPENDIX A: DERIVATION OF UNCERTAINTY IN TRUE SHADOW WIDTH (ΔS_{TRUE})

As discussed in Section 3.3, the uncertainty in the true shadow width (ΔS_{true}) depends only on the uncertainties in the observed shadow width (ΔS_{obs}) and the obliquity of the satellite parallel to the Sun's line of sight ($\Delta\varepsilon_{\parallel}$). Hence, ΔS_{true} is given by equation (A1).

$$\Delta S_{\mathrm{true}} = \sqrt{\Delta S_{\mathrm{obs}}{}^2 \left(\frac{\partial S_{\mathrm{true}}}{\partial S_{\mathrm{obs}}}\right)^2 + \Delta\varepsilon_{\parallel}{}^2 \left(\frac{\partial S_{\mathrm{true}}}{\partial \varepsilon_{\parallel}}\right)^2} \quad \text{(A1)}$$

$\Delta\varepsilon_{\parallel}$ can be found by knowing the range of possible ε values given the size of the image and using equation (A2).

$$\begin{aligned}\Delta\varepsilon_{\shortparallel} &= \Delta\varepsilon\left(\frac{\partial\varepsilon_{\shortparallel}}{\partial\varepsilon}\right)\\ &= \Delta\varepsilon\left(\frac{\partial}{\partial\varepsilon}\left[\arctan\left(v/d_h\right)\right]\right)\\ &= \Delta\varepsilon\left(\frac{\partial}{\partial\varepsilon}\left[\arctan\left(|\cos\gamma|\tan\varepsilon\right)\right]\right)\\ &= \Delta\varepsilon\left(\frac{|\cos\gamma|\sec^2\varepsilon}{\cos^2\gamma\tan^2\varepsilon+1}\right).\end{aligned} \tag{A2}$$

In case (A), where $0^\circ < \gamma < 90^\circ$, $S_{\rm true}$ is given by equation (17) and the uncertainty is derived by the following.

$$\begin{aligned}\frac{\partial S_{\rm true}}{\partial S_{\rm obs}} &= \frac{\partial}{\partial S_{\rm obs}}\left[\frac{S_{\rm obs}}{\cos\varepsilon_{\shortparallel}}+\frac{S_{\rm obs}\tan\varepsilon_{\shortparallel}}{\cos\varepsilon_{\shortparallel}(\tan\alpha-\tan\varepsilon_{\shortparallel})}\right]\\ &= \frac{1}{\cos\varepsilon_{\shortparallel}}\left(1+\frac{\tan\varepsilon_{\shortparallel}}{\cos\varepsilon_{\shortparallel}(\tan\alpha-\tan\varepsilon_{\shortparallel})}\right)\\ \frac{\partial S_{\rm true}}{\partial\varepsilon_{\shortparallel}} &= \frac{\partial}{\partial\varepsilon_{\shortparallel}}\left[\frac{S_{\rm obs}}{\cos\varepsilon_{\shortparallel}}+\frac{S_{\rm obs}\tan\varepsilon_{\shortparallel}}{\cos\varepsilon_{\shortparallel}(\tan\alpha-\tan\varepsilon_{\shortparallel})}\right]\\ &= S_{\rm obs}\left(\frac{\partial}{\partial\varepsilon_{\shortparallel}}\left[\frac{1}{\cos\varepsilon_{\shortparallel}}\right]+\frac{\partial}{\partial\varepsilon_{\shortparallel}}\left[\frac{\tan\varepsilon_{\shortparallel}}{\cos\varepsilon_{\shortparallel}(\tan\alpha-\tan\varepsilon_{\shortparallel})}\right]\right)\\ &= \frac{S_{\rm obs}}{\cos\varepsilon_{\shortparallel}}\left(\frac{\sin\varepsilon_{\shortparallel}}{\cos\varepsilon_{\shortparallel}}+\frac{\sec^2\varepsilon_{\shortparallel}}{\cos\varepsilon_{\shortparallel}(\tan\alpha-\tan\varepsilon_{\shortparallel})^2}\right.\\ &\quad\left.+\frac{\sin\varepsilon_{\shortparallel}\tan\varepsilon_{\shortparallel}}{\tan\alpha-\tan\varepsilon_{\shortparallel}}+\frac{\sec^2\varepsilon_{\shortparallel}\tan\varepsilon_{\shortparallel}}{(\tan\alpha-\tan\varepsilon_{\shortparallel})^2}\right).\end{aligned}$$

In case (B), where $90^\circ < \gamma < 180^\circ$, $S_{\rm true}$ is given by equation (19) and the uncertainty is derived by the following:

$$\begin{aligned}\frac{\partial S_{\rm true}}{\partial S_{\rm obs}} &= \frac{\partial}{\partial S_{\rm obs}}\left[\frac{S_{\rm obs}\sin\alpha}{\cos\left(90^\circ-\alpha-\varepsilon_{\shortparallel}\right)}\right]\\ &= \frac{\sin\alpha}{\cos\left(90^\circ-\alpha-\varepsilon_{\shortparallel}\right)}\\ \frac{\partial S_{\rm true}}{\partial\varepsilon_{\shortparallel}} &= \frac{\partial}{\partial\varepsilon_{\shortparallel}}\left[\frac{S_{\rm obs}\sin\alpha}{\cos\left(90^\circ-\alpha-\varepsilon_{\shortparallel}\right)}\right]\\ &= S_{\rm obs}\sin\alpha\left(\frac{\partial}{\partial\varepsilon_{\shortparallel}}\left[\frac{1}{\cos\left(90^\circ-\alpha-\varepsilon_{\shortparallel}\right)}\right]\right)\\ &= S_{\rm obs}\sin\alpha\left(\frac{\sin\left(90^\circ-\alpha-\varepsilon_{\shortparallel}\right)}{\cos^2\left(90^\circ-\alpha-\varepsilon_{\shortparallel}\right)}\right).\end{aligned}$$

It is possible, albeit highly unlikely, that γ could equal exactly 0°, 90°, or 180°. If $\gamma = 0$ or 180°, $\varepsilon_{\perp}$ will be zero, meaning that $\varepsilon_{\parallel} = \varepsilon$ and $\Delta\varepsilon_{\parallel} = \Delta\varepsilon$. This means that equations (17) and (19) would reduce to those used by Cushing et al. (2015) if $\gamma = 0^\circ$ or 180°, respectively. However, $\varepsilon_{\parallel}$ will be zero if $\gamma = 90^\circ$ meaning that there would be no distortion in the shadow width (i.e. $S_{\rm true} = S_{\rm obs}$ and $\Delta S_{\rm true} = \Delta S_{\rm obs}$).

This paper has been typeset from a TEX/LATEX file prepared by the author.